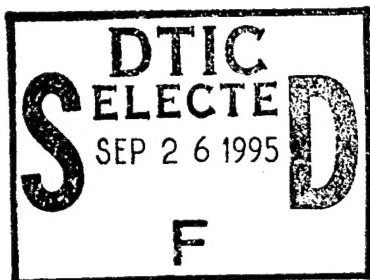


HTS FOR ELECTRONIC WARFARE APPLICATIONS



FINAL REPORT

CONTRACT NO. N00014-91-C-0199

Prepared for:

Office of Naval Research
800 North Quincy Street
Arlington, VA 22217-5000

Prepared By:

TRW Space & Electronics Group
One Space Park
Redondo Beach, CA 90278

DISTRIBUTION STATEMENT A

Approved for public release
Distribution Unlimited

22 September 1994

19950922 063

The views and conclusions contained in this document are those of the authors and should not be interpreted as necessarily representing the official policies, either expressed or implied, of the Defense Advanced Research Agency of the U.S. Government.



HTS FOR ELECTRONIC WARFARE APPLICATIONS FINAL REPORT

Table of Contents

1. Summary.....	3
2. Electronic Warfare Applications.....	7
2.1. Special Requirements.....	9
2.2. Electronic Warfare Discussion.....	10
2.3. Modern Electronic Warfare and Electronic Combat Architecture.....	12
2.5. Basic RF Components Required By The EW Architecture	16
3 HTS Deposition Techniques.....	19
3.1 Large Area Films.....	19
3.2 50 Ohm Resistor.....	22
3.2. Dielectric Films	23
4. Circuit Development	25
4.1 HTS 90° Hybrid Lange Coupler Circuit Design and Test.....	27
4.2 Broadband HTS Power Divider/Combiner Design and Test.....	37
4.3 Monopulse Beam Forming Network.....	41
4.4 Design Considerations for an HTS/Ferroelectric Phase Shifter	46
5. Cryocooler Subsystem Demonstration	67
5.1 Cryocooler Operation.....	67
5.2 Beam Steering Demonstration.....	69
6 Further Developments.....	78

Accession For	
NTIS CRA&I	<input checked="" type="checkbox"/>
DTIC TAB	<input type="checkbox"/>
Unannounced	<input type="checkbox"/>
Justification	
By <i>per ltr</i>	
Distribution /	
Availability Codes	
Dist	Avail and/or Special
A-1	

HTS FOR ELECTRONIC WARFARE APPLICATIONS

1. Summary

This final report describes the results achieved on the High Temperature Superconductors for Electronic Warfare Applications program. The objective of this program was to demonstrate beamforming network (BFN) components using High Temperature superconductors (HTS) operating between 50 and 70 K from 2-18 GHz intended for Electronic Warfare (EW) subsystems for early insertion. In particular, this program addressed three tasks; the first task developed the HTS processes required for the beamforming application, large area deposition, HTS compatible resistor process, dielectric film development for HTS overlay connections and ferroelectric phase shifters. The second task developed a number of components, including a broadband 90° hybrid, a power splitter, a broadband phase shifter, and a beamforming network. The final task developed cryogenic packaging techniques and demonstrated a component (a phase shifter) on a cryocooler.

The approach was to define process requirements required for HTS microwave circuits. Once the process requirements were defined, we developed the HTS processes: large area (5 cm diameter) coverage, resistor elements, dielectric layers. Next, specific microwave circuits were designed and demonstrated: broadband 90° hybrid, power splitter, and a beamforming network. Finally, we demonstrated a microwave subsystem (a two element phased array antenna) on a compact closed-cycle cryocooler.

All objectives of the program were achieved.

- Demonstrated broadband 100 MHz to 20 GHz HTS/ferroelectric phase shifter with HTS CPW circuit covered with a ferroelectric film.
- Developed a method to calculate the effective dielectric constant ϵ and loss tangent for a multilayer CPW structure.
- Demonstrated a 50 Ω /square resistor using NbN for use with YBCO microwave circuits.
- Designed and tested a broadband power splitter for EW BFN applications. The power splitter design uses the microwave thin film 50 Ω /square resistor developed on this program.
- Provided a monopulse and a power splitting BFN design for HTSSE-II program sponsored by NRL.
- Demonstrated the design, fabrication, and test of an HTS 90° hybrid. Showed >2:1 bandwidth and a 60% improvement over an all Ag circuit.

Demonstrated capability of fabricating Lange couplers with bond wires between fingers of the circuit

- Demonstrated beam steering with an HTS/ferroelectric phase shifter integrated with a closed-cycle cryocooler.

On a rudimentary level, many electronic warfare subsystems consist of an array of antennas which feed phase shifters and power splitters as shown in the block diagram of Figure 1-1. This sort of array can be implemented by an HTS broadband beamforming network which feeds a set of continuously variable, low loss phase shifters which enable AZ/EL beam steering, as sketched in Figure 1-2. Important elements of this subsystem (power splitters and HTS/ferroelectric phase shifters) were developed under this program. The innovative HTS/ferroelectric phase shifter developed and demonstrated by this program exhibited excellent performance, as shown in Figure 1-3. The operation of this continuously variable phase shifter is schematically shown in Figure 1-4. By integrating the phase shifter on a cryocooler, we were able to demonstrate beam steering, Figure 1-5. The most exceptional feature of this phase shifter is its extremely broad bandwidth. The phase shifter easily meets the full 2-18 GHz bandwidth required for EW applications, as demonstrated by the data in Figure 1-6.

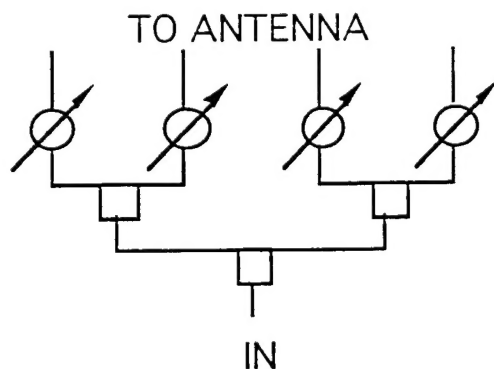


Figure 1-1. A general example of a beamforming network with power splitters and phase shifters useful for many EW applications.

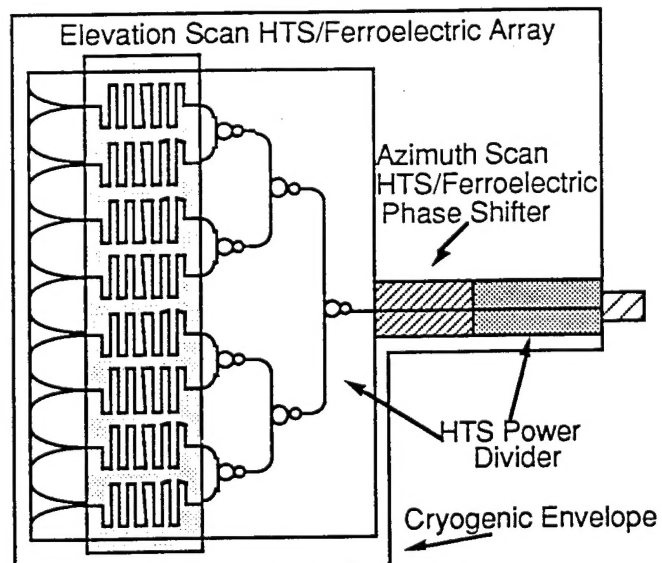


Figure 1-2. Sketch of phased array antenna with beamforming networks and phase shifters. The power splitters and phase shifters have been developed under this program

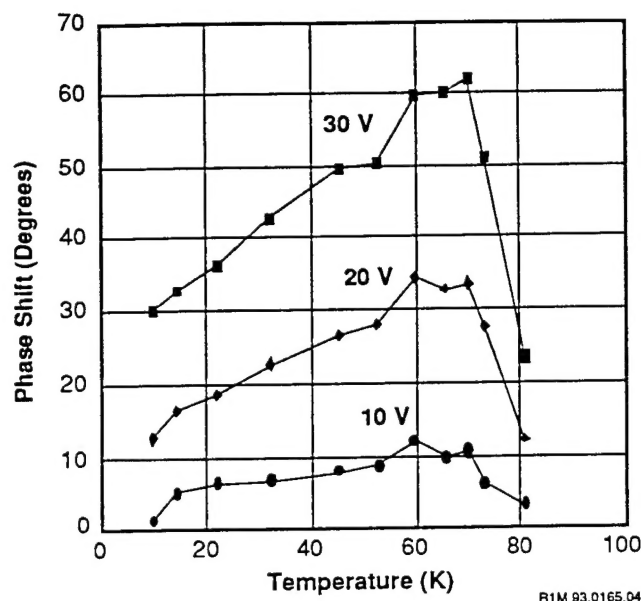


Figure 1-3. Recent data on an HTS / Ferroelectric phase shifter at 60 K at 10 GHz for a 1 cm length device.

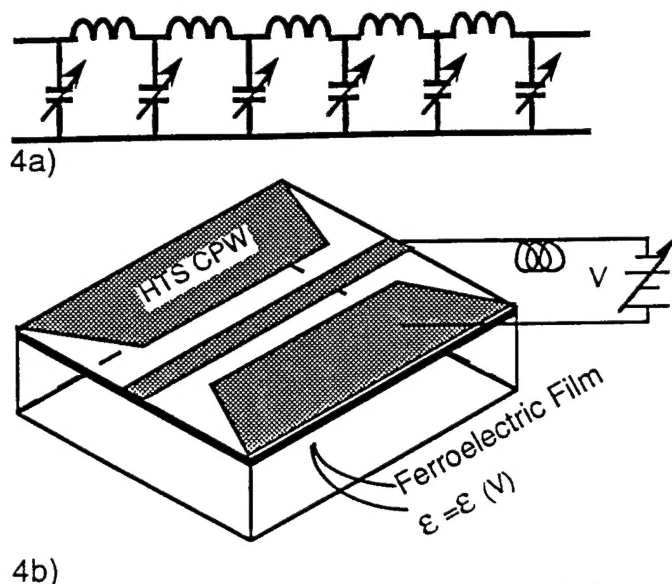


Figure 1-4. HTS/Ferroelectric phase shifter combines low loss with voltage tunable phase velocities. 4a) shows how a variable capacitance per unit length enables the phase shift, while 4b) shows how the bias voltage is connected.

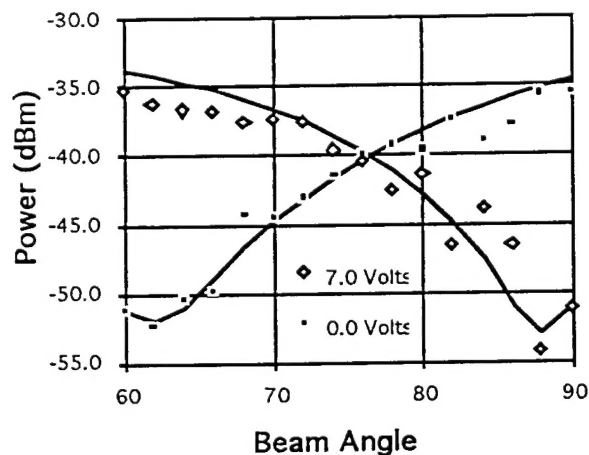


Figure 1-5. Beam angle at two control settings. An HTS/ferroelectric phase shifter, integrated on a closed-cycle cryocooler, demonstrated beam steering

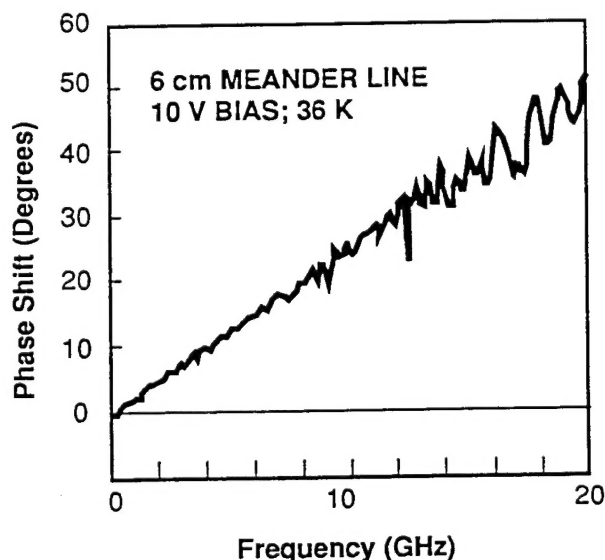


Figure 1-6. HTS/Ferroelectric phase shifter has true time delay performance up to 20 GHz, covering the entire 2-18 GHz EW band.

The problems presented by the limited bandwidth of conventional components, the moderate to high losses between antennas, the high cost of phased array antennas, and the non-reciprocal ferrite phase shifters can be solved by the use of HTS. HTS offers benefits because it:

- Minimizes aircraft installation problems with a single broadband array .
- Enables implementation of lower cost compact arrays
- Reduces phased array cost and simplifies control
- Improves ECM depth, reduced resolution time and reduces control complexity

This program concludes that future work to develop wideband multilayer directional couplers, to further develop the broadband HTS/ferroelectric phase shifter, and to develop new digital applications of superconductive electronics is required to fully offer the benefits of HTS to Electronic Warfare systems.

2. Electronic Warfare Applications

Since its discovery in 1986, high temperature superconductivity (HTS) has offered the potential for improved electronic warfare system performance. HTS materials have the potential for improvements in both RF analog circuits and high speed digital processing circuits. The HTS circuits will provide lower loss, reduced size, and lower power requirements. Since HTS requires cooling to 77 K, the cryogenic cooling demand are significantly reduced over the 10 K required for low temperature superconductors. Fortuitously, closed cycle cryogenic technology needed for HTS is now flightworthy because it has been developed for IR applications.

Components	Phased Array	Polarimeter	Passive BFN
1-Phase Shifter 2-Broadband Power Divider 3-90° Hybrid These three components are essential for the three different subsystems			
Properties	<ul style="list-style-type: none"> •Low Insertion loss •Wide Bandwidth •Low Power •Beam Steering 	<ul style="list-style-type: none"> •Low Insertion loss •Wide Bandwidth •Low Power •Polarization Control 	<ul style="list-style-type: none"> •Low Insertion loss •Wide Bandwidth •Low Power •Phase Linearity/ Beam Quality
Avionic Applications Benefits	<ul style="list-style-type: none"> •Cost Reductions Due to Low Cost Phase Shifter •Reduced Aperture Size Due to Broad Bandwidth and Low Loss •Vernier capability Eliminates Scalping Losses 	<ul style="list-style-type: none"> •Cost Reductions Due to Low Cost Phase Shifter •Reduced Aperture Size Due to Broad Bandwidth and Low Loss •Reciprocal Operation is an Added Benefit 	<ul style="list-style-type: none"> •Reduces Size •Improves Performance •Supports Phased Array and Polarimeter •Supports HTSSE-II

Figure 2-1. HTS EW Demonstration Subsystems

Since the key analog elements of a EW system are the phase shifter, the broadband power combiner/splitter, and the 90° hybrid, HTS versions of these components were chosen for design, analysis, and test. These three elements can form many useful EW

subsystems, as shown in Figure 2-1. The range of problems and potential payoffs benefiting by these technical objectives is summarized in Figure 2-2.

Problem	Technical Objective	Payoff
Limited bandwidth of conventional components results in "Antenna Farms" and large group A impact	Develop HTS components with 10:1 Bandwidth	Single broadband array minimizes aircraft installation impact.
Losses preclude microstrip components at mm-wave frequencies, between array elements, or before amplifiers	Develop low loss array components	Enables implementation of lower cost compact arrays
High cost of phased array antennas	Develop continuously variable HTS phase shifter	Reduces phased array cost and simplifies control
Non-reciprocal ferrite phase shifters used in anti-monopulse ECM require calibrations	Develop reciprocal low loss HTS phase shifter	Improves ECM depth, reduced resolution time and reduces control complexity

Figure 2-2. Range of problems and potential payoffs of HTS.

The benefits of beamforming networks for broadband, low cost, true-time delay phased arrays, are shown in Figure 2-3. Phased arrays will lead to tactical ECM arrays for fighter aircraft, stand-off jammers, arrays for high performance SIGINT aircraft, radar arrays for fire control, and missile approach warning. Low loss array components will lead to 2-18 GHz and mm-wave receive arrays, ECM arrays, and radar arrays. Low loss reciprocal phase shifters will make impacts on High Performance Anti-Monopulse ECM applications such as cross-polarization techniques of Cross-Eye and Double-Cross and high performance sidelobe cancellation.

Two HTS microstrip circuits were designed and tested using a specially designed test jig and showed the lower loss expected of HTS circuits but also pointed out the critical design problems that the HTS analog microstrip design process encounters due to the high dielectric constant and granularity of the LaAlO_3 substrate.

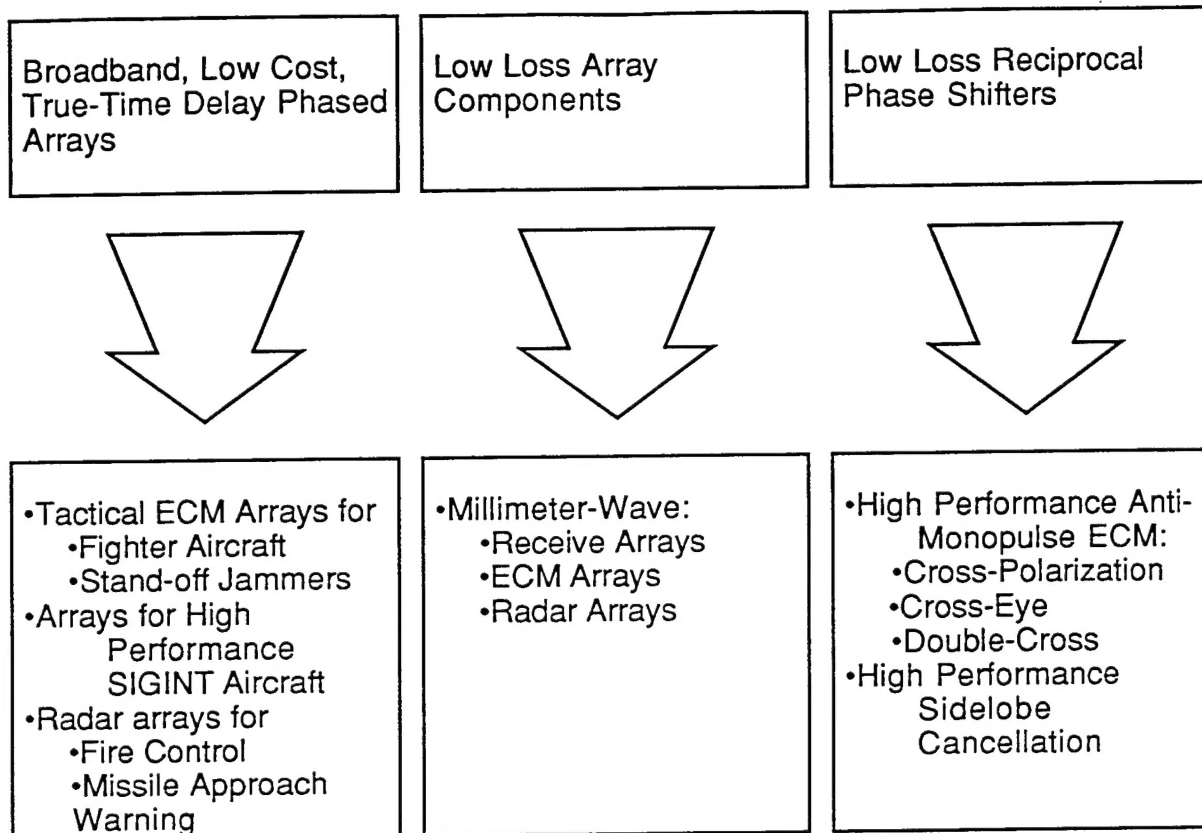


Figure 2-3. Spectrum of HTS Applications to Advanced EW Systems

2.1. Special Requirements

The special requirements of EW processing, characterized by wideband-wide field of view antennas, wideband-high dynamic range analog processing, and high speed digital signal processing, can benefit from the low RF loss provided by HTS microstrip circuits. These HTS RF circuits are smaller, have higher Q (and the resulting sharper filter characteristics), and have little frequency dispersion (resulting in wider bandwidths). Using coplanar waveguide, stripline, and microstrip circuits, complex analog HTS preprocessors that are much smaller than room temperature counterparts can be fabricated.

The availability of small EW HTS analog preprocessors would allow them to not only be placed in aircraft but also to be used in missiles such as the Tomahawk, TSSAM, and the Tacit Rainbow. They could also be deployed in unmanned air vehicles (UAV's) as part of a low cost ESM system.

2.2. Electronic Warfare Discussion

Electronic warfare is conducted to increase the probability of mission success and survival of friendly attacking forces and to decrease these probabilities for unfriendly forces. The early deployment of early warning and ground control radars by the British during the second world war significantly reduced the probability of mission success and mission survival of the attacking German aircraft even when they used a coordinated mass attack strategy. The effective counter measure, curiously given up by the Germans when almost successful, was to bomb the radar stations. This is still the most effective EW counter and its modern implementation is done through the use of the HARM (AGM-88) missile, the TACIT RAINBOW (now canceled) missile, and other cruise missile types. When this approach is not possible, a set of increasingly complex electronic techniques are employed to prevent detection and tracking by unfriendly radars and IR sensors. If tracking is accomplished and SAM's are launched, the deployment of decoy expendables is the endgame technique.

To choose the most effective countermeasure, a high fidelity situation assessment of the force deployment on the battlefield must be maintained in real time. This requires a wideband, wide field of view EW system capable of detecting and characterizing (in terms of lethality and intent) the many waveforms that are present on the battlefield. There is a modern emphasis on the increased use of unmanned air vehicles (UAV's) for attack, so the classical requirement for a high probability of mission survival has been reduced. Figure 2-4 shows the block diagram of the modern EW system architecture. This block diagram shows a modern EW processing scheme that uses a wideband-wide field of view antenna, a wideband modeformer, sub-octave RF processing, narrowband super heterodyne receivers that are frequency cued by the signals from the channelized filter. The system analyzes incoming signals and jams those that are lethal using signals derived from a digital RF memory (DRFM). The jamming antenna system is a high gain, wideband, steered beam array that allows the effective radiated power of the jamming to be high. Expendables are dispersed as a last resort under the direction of the central processing unit (CPU). The entire system is calibrated in real time using aperture injection of coherent calibration signals.

Coherent Processing Requirements

In order to perform all of the required EW functions, the system must be capable of sophisticated coherent processing. This processing has particularly difficult bandwidth and dynamic range requirements. Since the EW electronic environment often

includes many high power jamming sources, the system must detect weak signals in the presence of very strong ones; jamming and signals of interest may differ by 100 dB. This places severe requirements on filter shapes, device linearity, and the frequency plan. As is shown in Figure 2-4, the requirements cannot be met without a sub-octave frequency plan where the non-linear active elements are placed after sub-octave filters that usually split the 2- 18 GHz band into 2-3.5 , 3.5-6, 6-10, and 10-18 GHz.

Some advanced work is directed at replacing all of the analog RF circuitry shown in Figure 2-4 by a fast analog to digital converter (A/D); however, no state-of-the-art A/D that is fast enough can provide more than about 50 dB of dynamic range so that amplitude channel splitting is required and the architecture becomes complex.

In a complex electronic environment, pulses arrive at the antenna at a mega- pulse per second rate and must be characterized and associated with threat systems. The pulses often fall on top of each other (pulse-on-pulse or POP) and may have frequency and amplitude modulation on pulse (MOP). This environment provides a challenging coherent processing problem. To solve the problem and keep costs low, the receiver is built up of wideband receivers and fast tuned narrowband superheterodyne receivers. The narrowband receivers are "cued" by the wideband receivers that detect threats in a 50 MHz bandwidth. They tune to the threat frequency and receive the delayed (via a SAW or HTS delay line) pulses. Once digitized, the frequency, amplitude, pulse width, and time of arrive are processed by a parameter encoder and passed to a digital processor for identification and situation assessment. The high pulse densities and the need to react quickly to waveform changes place throughput requirements on the parameter encoder/preprocessor that are in the billions of operations per second range.

Threats are identified and associated with a weapons system, and assessed for lethality and intent so that electronic counter measures can be employed. HTS has the potential to reduce the size of all of the microstrip RF circuits used in this architecture and possibly to increase the speed of the digital A/D conversion and the digital preprocessing. The main advantage of HTS is its ability to miniaturize extra-wideband RF circuitry, provide improved RF circuit performance, and to provide high speed digital processing at very low power.

The diagram illustrates the architecture of the A-1000 signal processing system. It features two main input paths: RCP MASA (Right Channel Path Main Antenna Subsystem) and LCP MASA (Left Channel Path Main Antenna Subsystem). Both paths include a 10:1 4X4 MFN (Main Frequency Network) and a CAL (Calibration) input. The signals are processed through a series of sub-octave preselection, amplifiers, and band switches. The RCP path includes M3RCP, M1RCP, and M2RCP stages, while the LCP path includes M3LCP, M1LCP, and M2LCP stages. These signals are then routed through EX1 switches and a CROSSBAR SWITCH to a FAST-TUNED SUPERHET RECEIVER. The receiver outputs are connected to a CHANNELIZED RECEIVER, which provides CUES INFORMATION to a PREPROCESSOR. The PREPROCESSOR is connected to a CPU, which in turn is connected to a TIMING CONTROL. The CPU also interfaces with a BIT/CAL block. The system is controlled by an EXPENDABLE IR/RF/EO (Infrared/Radio Frequency/Extensible Optics) unit, which is connected to an IR/EO input and a DISPLAY. The DISPLAY shows a graphical representation of the signal processing results.

Antenna System

filters. This antenna system would provide about 3 dB improved sensitivity and would be much smaller in size.

Preprocessor

The multiple arm spiral antenna system is most effective when coupled to a high speed preprocessor that sorts threats based on their azimuth angle. This can be achieved by sorting on the basis of mode ratio phase from the modeformer. While this is usually done digitally, a low loss HTS analog version might be possible and provide the needed throughput.

Beam Forming (Field of View Channelizing)

Two types of beamformers are needed for the EW system shown in Figure 2-4, a true time delay beam former to steer the ECM antenna system beams, and a constant phase beam former to select signals coming from a specific direction that enter the multiple arm spiral antennas. Paul Ryan has reported (P. Ryan, " High-Temperature Superconductivity for EW", Journal of Electronic Defense, August, 1992) that a true time delay (2-6 GHz) HTS delay line was developed by Westinghouse in 1992 and showed excellent constant time delay across the entire band of interest. Improved devices are commercially available from Superconducting Technologies, Inc.

Frequency Channelizing

The frequency channelizing function (usually part of the medium band receiver) performs a splitting of the fundamental 2-3.5, 3.5-6, 6-10, 10-18 GHz bands into 50 MHz wide subbands. These "channels" are then monitored for activity and a fast-tuned narrowband receiver tuned to search the 50 MHz band and to track the threat signal. In a cued receiver architecture the coherent pulse signals coming from the medium band receiver are delayed in a delay line until a narrowband receiver can be tuned to intercept them.

HTS technology offers the possibility of producing higher Q filter stages and providing the associated steeper sloped filters. An HTS channelized filter would therefore have higher interchannel rejection and lower losses. P. Ryan shows an HTS 6-pole filter with 150 MHz bandwidth, < 1 dB of insertion loss, and 60 dB out of band rejection. The HTS filter shows about 20 dB greater rejection than an identical gold filter.

The delay line needed to delay channelized pulses so that they can be detected by the narrowband receiver needs to have a dispersion free, 10 μ s delay to allow for the

tuning time of the receiver. State-of-the-art HTS delay lines of 100 ns have been reported so that an increase of the delay time of 100 is required to support the cueing function.

Cued Narrowband Receiver

The cued narrowband receiver, while more complicated, can detect burst mode radars since it can get threat information on a single pulse. The pulse is video detected by the medium band receiver and a frequency measurement made. This information is sent to the fast tuned narrowband receiver controller and the receiver is tuned to the correct frequency to await the appearance of the pulse at the delay line output. The narrowband receiver detects the pulse with high sensitivity, digitizes the information and passes it to the Parameter Encoder that assembles a pulse descriptor word that is sent to the preprocessor.

The key to a high performance narrowband receiver is a low phase noise, fast tuned synthesizer. A mix and divide synthesizer referenced to a standard crystal reference using superconducting digital circuits can meet the requirements. The cross-band tuning speed of 10 ns would allow the associated "cueing" delay line to be shorter. Surface Acoustic Wave (SAW) resonators. Browne shows (J. Browne, "SAW Devices Set Long Term Stability Marks", *Microwaves & RF*, May 1994) that a 500 MHz SAW (from Raytheon) can have a phase noise of -140 dBc/Hz @ 1 KHz from the carrier. The SAW substrate is reported to be aluminum oxide.

Digital Processor

Electronic warfare processing cannot take place without high throughput digital processing. Some directorates of the Wright Laboratories are even suggesting an all digital EW receiver where a high speed A/D converter is connected almost directly to the antenna. Such an architecture requires billions of operations per second so that HTS digital processing is the only feasible low power solution. A pipeline HTS digital preprocessor could provide high throughput in a small package.

State-of-the-art superconducting counters are limited to frequencies below 80 GHz. Improvements in fabrication technologies and optimization of the counter designs should permit these frequencies to increase to about 200 GHz with an ultimate physical limit above 500 GHz. In this mode of operation, the A/D converter resolution is determined by the maximum number of pulses the counter can accumulate in the time between samples. The practical limit is set by a counter frequency of 200 Ghz

which will be obtainable largely due to fabrication process improvements. The chip power is about 20 micro Watts.

Parameter Encoder

An analog system, like that shown in Figure 2-4, requires a parameter encoder to translate the analog detector signals into a digital format. The TRW 4VPE parameter encoder chip receives analog (video) signals from four sources and provides a digital output of pulse amplitude, pulse width, time of arrival, and pulse characterization. The accumulated pulse amplitudes can be compared to the amplitudes in adjacent channels/sectors by means of an arbitration algorithm. Pulses that appear in multiple channels, which is often the case since the channelized filter requires some overlap, are sorted and the strongest version selected by the parameter encoder. When pulse frequencies land on the highly dispersive filter edges, the pulses exhibit a "rabbit-ear" phenomenon that must be arbitrated by the parameter encoder.

Electronic Counter Counter Measures (ECCM) System

An important part of the EW endgame is the efficient deployment of decoy expendables. Indeed for post-modern warfare a system that detected, classified, selected and deployed the correct threat decoy at the right time might be sufficient. If this deployment was transparent to the pilot, who usually has other things to do, the system would be even better. Prior to the decoy deployment some counter measure jamming might be employed.

Digital RF Memory

The digital RF memory stores the pulse characteristics of incoming radar pulses so that they can be retransmitted to mask the radar return from the platform. The delay (or latency) through such a system is critical so the radar detector cannot just take the first returning pulse. The digital RF memory must have high fidelity, high speed A/D's coupled to high speed memory so that the coherent properties of pulses can be stored. An HTS version of a digital RF memory would be smaller, use lower power, and have improved throughput.

An important complimentary portion of the digital RF memory is the D/A converter used to reconstitute the signal. TRW has successfully tested a 4-bit 1 GHz superconducting D/A. Within two years, a 10 GHz 6 to 8-bit D/A could be designed, fabricated, and tested.

High Power Waveform Generation

The generation of high power jamming based on waveforms generated by a digital RF memory will be best accomplished by TWT tubes and is unlikely to be a target for HTS technology.

Expendables IR/RF/EO

Infra-red and Optical flares are deployed to decoy missiles that have this type of sensors. These decoys are effective if deployed at 20-30 seconds "time-to-go" for the attacking missile.

The HTS technology may well have an important application to the RF decoy. Such a decoy must be small and would take advantage of the size reduction provided by HTS. The life time of such decoys is less than 1 minute so that onboard initial cooling would be all that is necessary. The RF decoy would provide an amplified return of the radar waveform used by the missile or ground control radar and thereby mask the platform. Power levels would not need to be high, but the decoy would need to follow the missiles frequency and PRF as it passed through its terminal guidance modes. Missiles and aircraft generally use medium PRF waveforms for target acquisition and transition to high PRF for terminal.

2.5. Basic RF Components Required By The EW Architecture

The basic analog components that are key components of the EW architecture shown in Figure 2-4 are the broadband 90° hybrid, the broadband power combiner/splitter, the channelizing filter, a phase shifter, and the analog delay line. The digital components that are key to electronic warfare are the high speed analog to digital converter and high speed pipeline preprocessing. For avionics systems, small size and compact packaging is an advantage.

Broadband Analog 90 Degree Hybrid

The 90° hybrid is characterized by its S matrix representation. These scattering parameters measure the effects of inputs on the four port device in terms of its transmitted and reflected voltages (50 Ω impedance assumed). The number of sections used in a broadband 90° hybrid increases with the bandwidth, while increasing the losses. Hence, HTS can provide substantial improvements in the insertion loss. Thin film approaches which suffer from increased insertion loss for normal metals can benefit by the use of HTS.

Broadband Analog Power Combiner/Splitter

The power combiner also benefits from the use of HTS for broadband applications. Thin film resistors are required for this component, and this program demonstrated that integrated thin film resistors are compatible with HTS processing.

Broadband Analog Phase Shifter

The analog phase shifter developed in this program is exceptional because of its ultra-broad bandwidth. No similar device exists, and the long term impact of this revolutionary device remains to be evaluated for electronic warfare systems.

Analog Channelizing Filter

A multichannelizing filter provides important signal separation, but in many applications the insertion loss of the filters has limited the subsystem design. HTS offers revolutionary implications for this device: lower loss, compact size, higher out-of-band rejection.

High Speed Digital Processing

HTS offers the possibility of low power extremely high speed digital processing. Its application to preprocessing will allow high throughputs at low power levels. The less than 100 nanowatts/ gate required by Josephson logic allows the construction of megagate circuits with minuscule power dissipation.

Analog to Digital Converter

High speed analog to digital converters are ultimately limited by the power/gate requirement of the logic used so that HTS logic offers the only technology capable of achieving a 12 bit 10 Gbps A/D converter. A miniaturized high speed HTS preprocessor that does parameter encoding and azimuth sector sorting could revolutionize airborne EW processing.

Pipeline Preprocessing

A pipelined high speed architecture offers the best application of HTS digital logic since it would provide billions of operations per second when running a limited but programmable set of algorithms. The programming complexity (no compiler or language exists) of this type of processor would be compensated by its blinding speed.

A typical pipeline architecture useful for coherent processing uses a vector architecture with 2 multipliers, 2 adders, and associated buffer memory making up a single "pipe". This architecture allows complex number-based algorithms to be run

synchronously. By assembling identical "pipes" in stages, the processor is made up of basic building blocks. About 6 pipes and 5 stages would be adequate for EW processing and is likely to produce a throughput of 60 Gops when clocked at a 1 GHz rate. The control and programming of the data flow is accomplished using digital data muxes between stages. The more complicated this control circuitry the more flexible and SLOWER is the processor.

Algorithms that flow through the processor without interruption are likely candidates. All EW preprocessor algorithms are of this type.

3 HTS Deposition Techniques

The objectives of this program were to develop the techniques required to manufacture wideband, low loss, microwave circuits. The initial requirement for microwave circuits had already been determined at the start of the program: patterning to within 5 μm tolerances. The project requirements were:

- to develop a technique to cover the entire surface of a large area wafer (5 cm in diameter).
- to demonstrate that thin film resistors (needed for microwave power splitters and terminations) were compatible with HTS processing. T
- to demonstrate bonding and crossover metallization for Lange couplers.
- to develop good SrTiO_3 thin films for an HTS/ferroelectric phase shifter.

Other important techniques including two-sided HTS film deposition, lower dielectric constant substrates, and the use of thin dielectric films which allow higher coupling are being developed at TRW and other locations under other programs.

The next sections describe the 5 cm diameter wafer deposition process, the thin film resistor process, and the bonding and crossover development that was accomplished under this program. The SrTiO_3 thin film work will be described in section 4.4.

3.1 Large Area Films

This section describes the work that was performed to demonstrate a large area (5 cm diameter wafer) deposition technique. The deposition geometry, Figure 3-1, shows the laser beam entering a vacuum chamber, incident on the target. The beam vaporizes the target material, and a plume of the YBCO material is ejected onto a heated substrate. To achieve large area coverage, the heated substrate is translated and rotated. A whole 5 cm wafer can be covered in the system, even though the center of the heater translational stage can only be moved about 4 cm.

Depositing YBCO uniformly on the rotating wafer is a non-trivial exercise in geometry since the exact plume density profile, an accurate dwell time at each radius, and choice of dwell settings must be optimized. A program was written to model the large area deposition process. The system was "calibrated" to coordinate the calculated radial positions to actual (x, y) positions of the heater translational stage. The

modeling program was then used to calculate the deposition radii and corresponding dwell times to produce a uniform film thickness over the 5-cm diameter area.

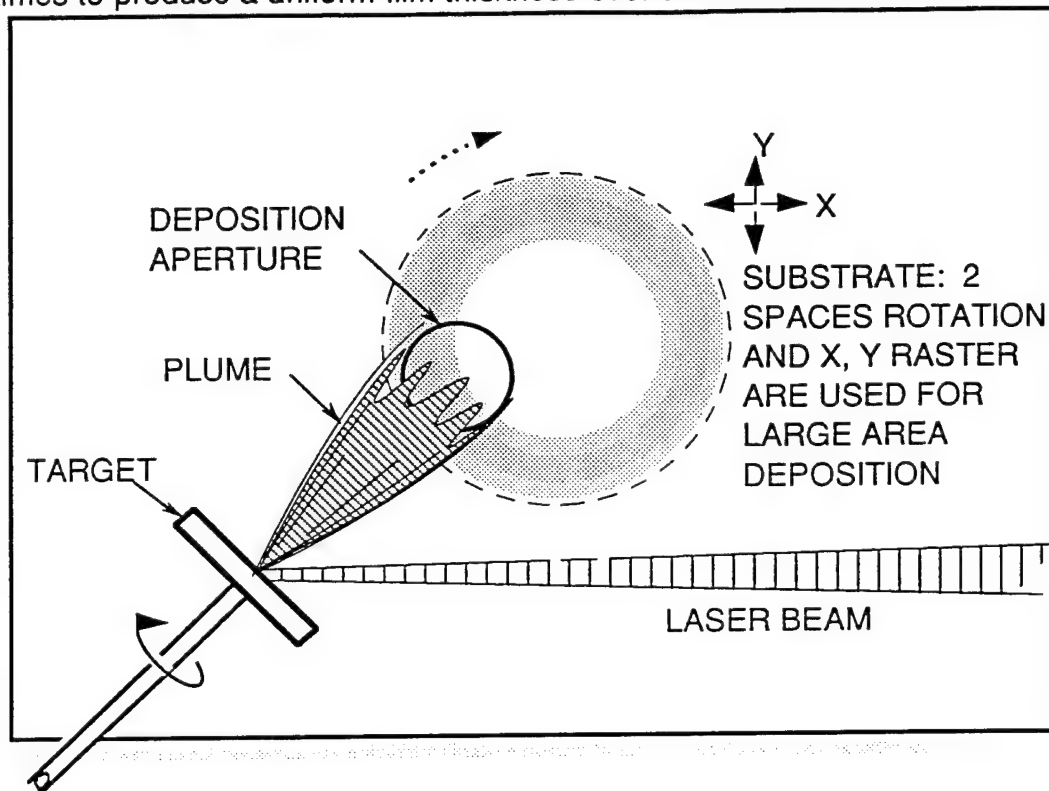


Figure 3-1 Schematic showing deposition geometry.

For example, when the plume center falls about 15 mm from the center of the substrate, we obtained a deposition profile such as the one shown in Figure 3-2. When the center of the plume was positioned at about 10 mm from the center of the substrate, a density profile across the wafer, such as the one shown in Figure 3-3 was obtained. By a proper combination of a total of 5 settings, we were able to obtain the uniform coverage of a wafer, shown in Figure 3-4. The falloff at the edges can be improved by including a larger deposition radius. The uniformity was 8%, with most of the variation due to the falloff at the edges.

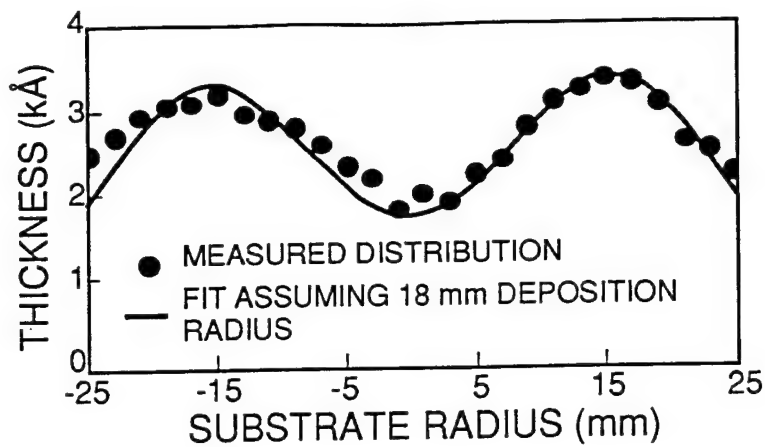


Figure 3-2. YBCO film distribution for rotating substrate at one radial position which is towards the outer side of the substrate.

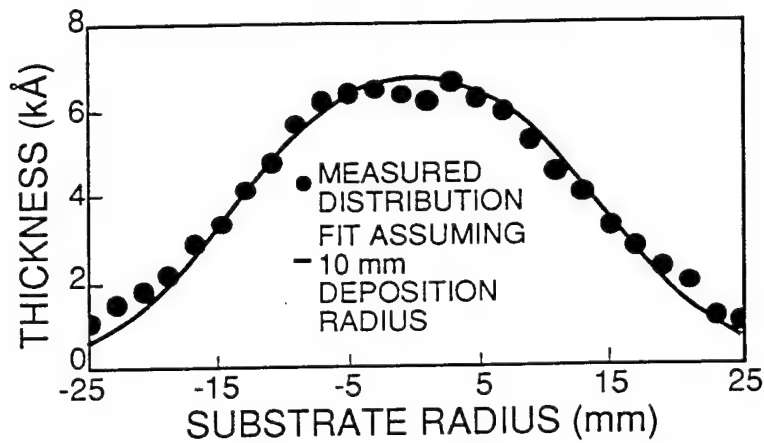


Figure 3-3. YBCO film distribution for rotating substrate at one radial position which is approximately 1 cm from the substrate center.

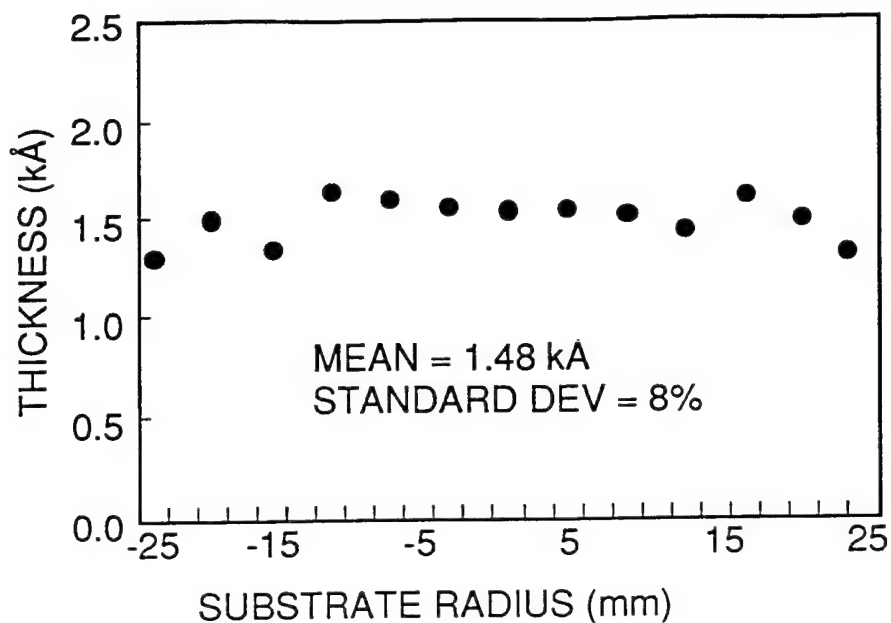


Figure 3-4. Large area coverage. A 5-cm wafer was covered with a 0.15 μm thick film of YBCO.

3.2 50 Ohm Resistor

The objective of the task was to develop a resistor technology which was compatible with HTS films. We chose two different resistor materials: NbN and Nichrome. The design goal was for a 50 Ω /square resistor with small variations over the wafer. The test structures incorporated in the development mask featured van der pauw tests, contact resistance tests, long line tests, and typical microwave resistor test patterns. Figure 3-5 shows a photograph of one cell of the mask.

A mature technology needs to implement a 4-step process where normal metal contact pads make contact to the HTS and to the resistor because the long term metallurgical interactions of YBCO and resistor materials are not known. Normal metals (Au and Ag) and HTS have been demonstrated to form stable contacts, but NbN and Nichrome may have long range metallurgical interactions.

The results of the development program are shown in table 1. The most difficult step in the resistor development project was to overcome contact resistances between adjacent Ag layers. For this reason, it is suggested that Au be used for the normal metal contact pads.

Process	Film Thickness	Target	Value
NbN (4 step process)	70 nm	50 Ω /square	50 Ω /square
NbN (2 step process)	78 nm	50 Ω /square	50 Ω /square
Nichrome (2 step process)	40 nm	50 Ω /square	50 Ω /square

Table 1 Results of the thin film resistor process development.

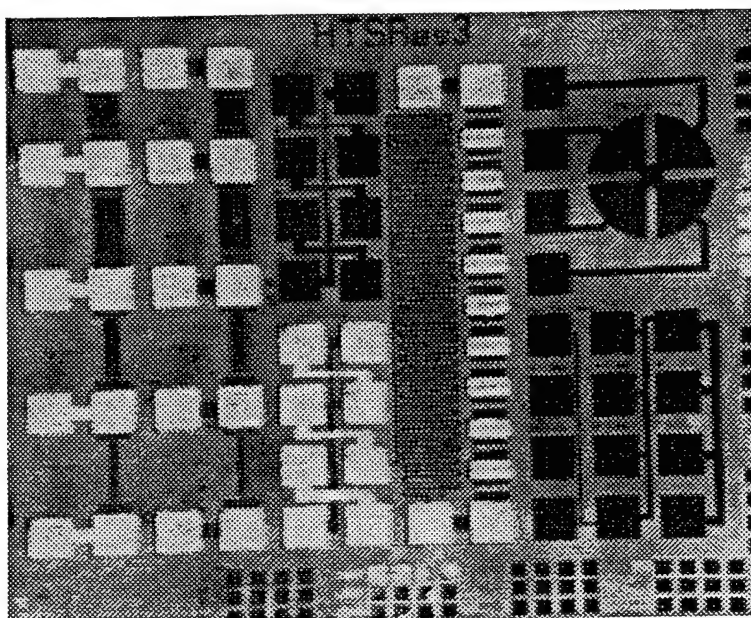


Figure 3-5 Photograph of one chip on the resistor development mask.

3.2. Dielectric Films

The need for dielectric films and crossovers comes from the requirements for Lange couplers. The bonding tests on working Lange couplers developed under this program will be shown in section 4.1 covering their performance. These wire bonds were successful in meeting the microwave design requirements, but more exacting design requirements exist, leading to Lange couplers with higher impedances (and smaller dimensions) which need smaller bonding pads.

We determined that for our process, bond pads smaller than 2-mils (50 μm) were too small to allow reproducible wire bonds with 1-mil (25 μm) wires. Use of Au instead of Ag bonding pads might enable more reproducible bonds, but more work in this area needs to be performed.

There is another point of view that leads to the conclusion that dielectric films with metallic crossovers are needed. Consider a complete monolithic monopulse BFN with 4 directional couplers which will require 48 bond wires. Clearly a process which makes all of the bonds with a reproducible process is more attractive than the bond wire approach.

A photograph of a test structure that was developed to test dielectric films and crossovers, Figure 3-6, shows a simple topological layout which simulates the requirements of a Lange coupler. After solving initial shorting problems related to photolithographic problems, the circuits demonstrated high yields.

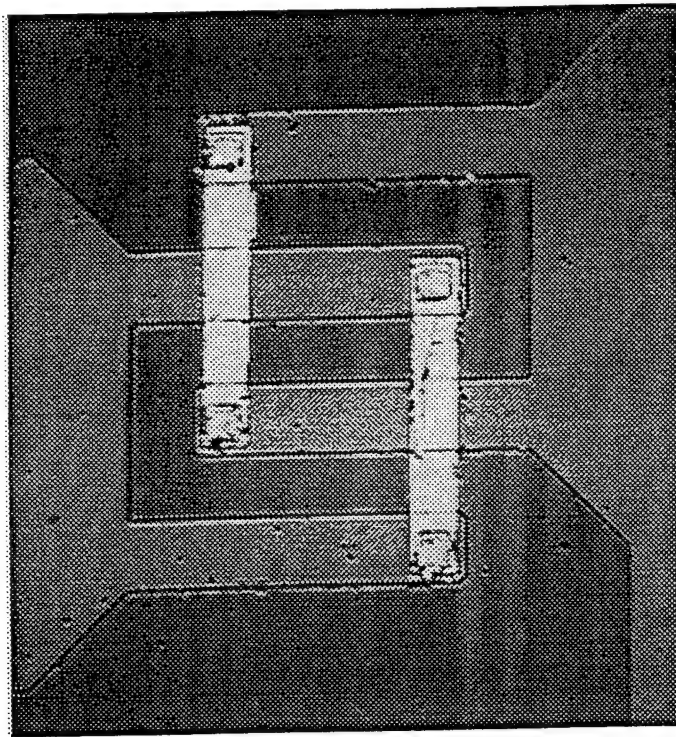


Figure 3-6 Photograph of the Lange coupler test development cell..

4. Circuit Development

Three circuits were developed: a 90° hybrid, a Wilkinson power splitter, and a broadband phase shifter. The sections which follow will describe their design, fabrication, and test.

The Approach

The approach taken under this program was to develop two processes that could be used to support the fabrication of HTS RF circuits using YBCO HTS films on a Lanthanum Aluminate (LaAlO_3) substrate. The LaAlO_3 substrate has the characteristics shown in Table 4-1.

Parameter	Value
Dielectric Constant	24.5
Loss Tangent	<.00003

Table 4-1. Lanthanum Aluminate Substrate (LaAlO_3) Characteristics

One approach used a 18 Ω microstrip circuit impedance and a 50 Ω to 18 Ω transformer and the other used a 50 Ω microstrip circuit impedance. The first approach could use wider line widths than the second, and was less susceptible to circuit linewidth and substrate thickness variations.

The advantage of HTS RF circuits was gauged using an identical non-superconducting silver/ LaAlO_3 circuit as a comparison. With both circuits cooled to 77 K, a comparative test could be performed. It should be noted that benefits were obtained even though only the microstrip line was superconducting; an Ag ground plane was used in all cases.

HTS Instrumentation and Test Procedure

A calibration test jig was designed and fabricated to measure the characteristics of HTS films at RF/mm-wave frequencies. This test fixture shown in Figure 4-1 can introduce errors, hence an accurate calibration must be performed to remove the effects of the test fixture. Since the devices being measured are electrically small and have low losses, the insertion loss improvement that HTS provides could be "washed" out due to mismatch loss or poor calibration. A trade study resulted in the choice of a popular test method, known as the TRL (through-reflect-line) method for our tests. This calibration technique is based on characterizing the transmission and reflection coefficients presented by the test fixture for known electrical length transmission lines

with high reflection coefficient, usually created by using an open-ended transmission line on the fixture. The fixture consists of two precision-machined, gold-plated blocks. Mounted on either one end of each of the blocks, are two Wiltron K-connectors that launch onto two microstrip transmission lines.

Two identical fixtures were constructed to speed-up calibration and testing. Two sets of transmission lines of known electrical length were fabricated on a Rogers 6010.5 substrate and inserted between the fixture blocks and measured. These measurements were then used in the calibration and allowed the required 2-18 GHz calibrated bandwidth to be achieved. Thermosonic bonding of three 0.7 mil ribbons for each transmission line path were required to get a high quality RF/mm-wave microwave connection. To improve the durability of the test fixture, molytaps striking pads are soldered to the ends of the transmission lines where the bonds occur. The TRL test fixture with an HTS Lange coupler is shown in Figure 4-1. The fixture is gold plated for corrosion resistance and to provide excellent RF grounding paths for the microstrip launchers. Alignment pins are used to guide the fixture halves together for repeatable, multiple mating and demating.

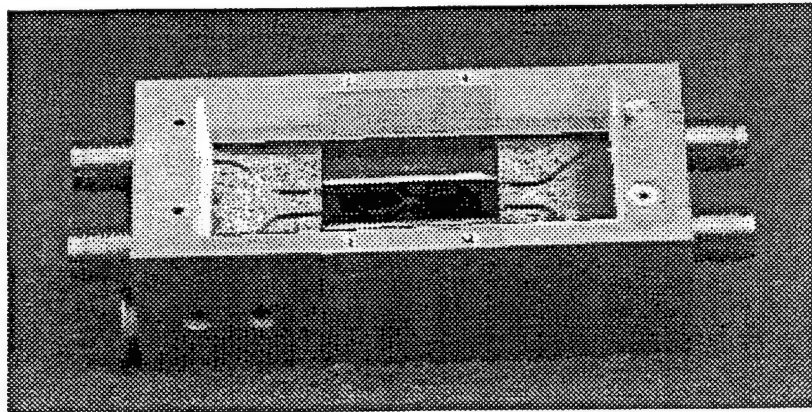


Figure 4-1 Photograph of TRL Calibration Test Fixture.

The stainless steel coaxial cables that interfaced the DUT and fixture to the automatic network analyzer were included in the calibration of the test fixture. Measurements of the test fixture showed a noticeable high frequency degradation. This was traced to one of the upper band transmission line standards being too long. Once corrected, calibrated operation up to 18 GHz was possible. Some of the early data presented in the following sections showing HTS improvement of component performance above 15 GHz should be ignored. Measurements of the input return loss of the TRL fixture

with TRL calibration show an improvement which is approximately 6-dB across the band of interest. This calibration decreases the interaction error of the test fixture and allows more accurate DUT measurements.

A dewar was used to lower the temperature of the DUT to that of boiling liquid nitrogen (77 K.) A vacuum was sustained at <14 milliTorr using a vacuum pump. Stainless steel coaxial cables were chosen for their high thermal resistance and to preclude raising the temperature of the fixture and cold plate within the dewar. These cables were used to transition the RF signals through the dewar from room temperature to the 77 K region. Indium shims were pressed between the fixture and the cold plate to reduce thermal resistance. The temperature was monitored using a diode sensor and maintained at <78 K. The diode sensor was fastened near the HTS RF circuit to assure accurate temperature measurements. Data was taken only after the dewar inside ambient temperature did not vary more than .25 K over 15 minutes. Future tasks should include an improved calibration procedure that would further decrease the interaction of the of the test fixture and the DUT.

4.1 HTS 90° Hybrid Lange Coupler Circuit Design and Test

The design of a broad band (>3:1), 3 dB coupler is limited by the available components. Table 4-2, lists of the performance goals for the HTS coupler.

Performance Parameter	Goal
Bandwidth	>3:1
Coupling	3 dB nom.
Amplitude Imbalance	± 1 dB
Phase Imbalance	± 3 degrees
VSWR	< 1.5:1
Isolation	> 15 dB

Table 4-2 Performance Goals for the HTS Coupler.

RF circuit components that could be combined to achieve these goals were characterized and the designs evaluated. The components considered included symmetric stepped quarter-wave section, asymmetric stepped quarter-wave section, branch-line, re-entrant, and interdigitated (Lange). In Table 4-3, the tradeoffs for the various coupler types are illustrated.

linear analysis program. The theoretical output power coupling for the two outputs of the Wilkinson power divider is shown in Figure 4-15.

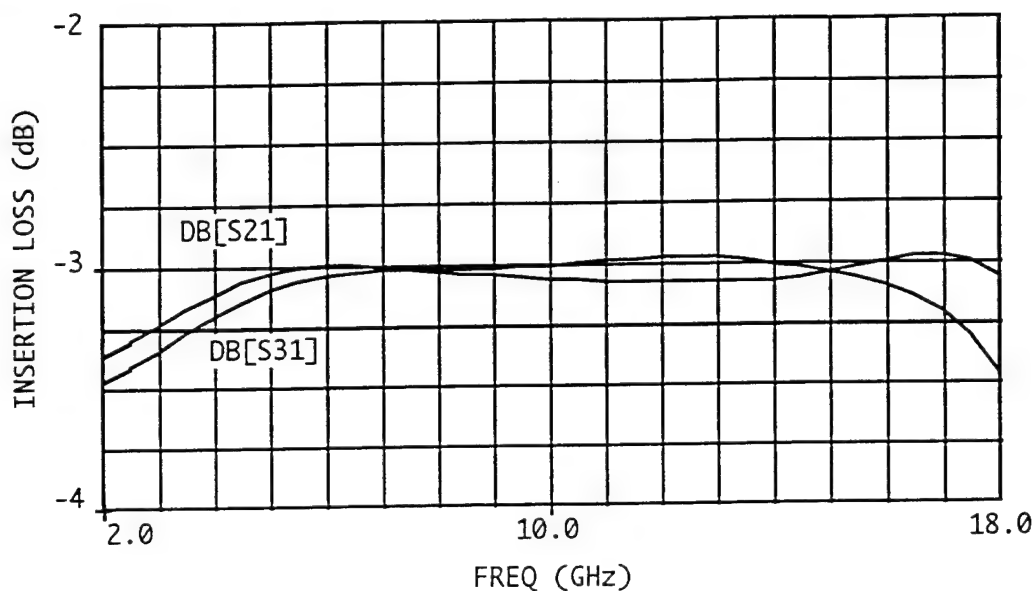


Figure 4-15. Theoretical Power Split Between Outputs of Wilkinson.

several observations were made during the testing stage of the HTS Wilkinson power dividers. The first was that the fabrication of the high impedance lines nearest the input was suspect. The lines were approximately 0.0002" (5 microns) in width. This is attributed to the resolution of the mask, based on a photographic process, as opposed to an e-beam mask. Of the four configurations that were fabricated only one worked. Of the three configurations that failed, all three devices were due to an open lines in the area where the highest impedance line (narrowest line) was fabricated. In Figure 4-16, the measured return loss of the PD-1 power divider is shown. The return loss indicates a 2:1 VSWR over a large portion of the band. One limitation on this measured performance was the microstrip launchers and the calibration process.

Figure 4-17 shows the measured insertion loss including the coupling loss for one of the Wilkinson Divider output ports. The operational bandwidth of the device is approximately 2 to 14 GHz. At about 10 GHz, a large "suckout" occurs in the passband due to a non-TEM mode of propagation that causes a large interfering signal to be summed with the incident signal. The insertion loss, including the 3 dB splitting loss, is approximately a constant 1 dB up to 10 GHz. The isolation was also measured indicating a good connection between the ohmic contact and the resistive NbN and good uniformity in the aspect ratio providing the correct resistance value. It is

Branch-line couplers are a planar structure that can be utilized to provide better than an octave bandwidth while still maintaining good phase and amplitude balance, but due to the bandwidth required by the HTS program, this device type was not considered.

Re-entrant mode couplers have the capability of large bandwidths at high coupling ratios. This technology utilizes dielectric films to equalize the even- and odd-mode phase velocity. The same problems exist with this device as the symmetric coupler.

Lange couplers are planar and can be implemented in a microstrip form. The interdigitated finger design compensates for the unequal even- and odd-mode phase velocities. Typical bandwidths for Lange couplers of 4- and 6-finger topologies are greater than an octave. With 8-finger Lange couplers analysis shows bandwidths of 3:1 can be achieved.

The Lange coupler was chosen as the baseline coupler. The Lange coupler design was based on a lower impedance level of approximately $18\ \Omega$ to achieve a high yield in the production of the circuit.

The overall length of the coupler is just under 0.7 inches. The coupler could be optimized and reduced in area if it were to be applied to a beamforming network design. Figure 4-3 shows the die artwork. The components at the top of the die are Lange couplers. The components below are back-to-back transformers that were used to evaluate the performance of the couplers. Special targets were used to verify alignment and photolithography accuracy. Test bonding areas were also included for perfecting the bonding technique and to allow bond pull tests. Figure 4-4, a sketch of the interdigitated section of the Lange coupler is illustrated. The line widths are 1.25 mils wide, with line-to-line spacing of 1.85 mils. This geometry falls within the bounds of high yield fabrication.

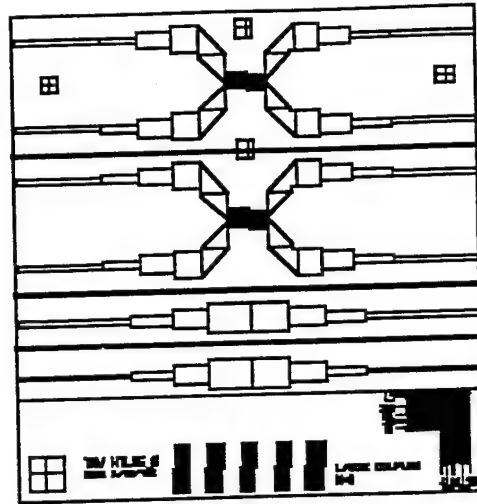


Figure 4-3. HTS Lange Coupler Die Artwork shows circuit size.

Figure 4-4, an enlargement of the Lange coupler features are shown. Gold bond wires are attached to the pads on the extreme left-end of the 2»4 and 5»7 fingers, extreme right-end of the 3»5 and 6»8, and in the middle section of the 1»3»5»7»9 fingers using thermosonic compression bonding techniques. Tests were performed on a set of bonding pads similar to the those test pads used on the test circuits. These tests were successful. The mean pull value was 2.7 grams. This figure falls within the minimum 2 gram limit.

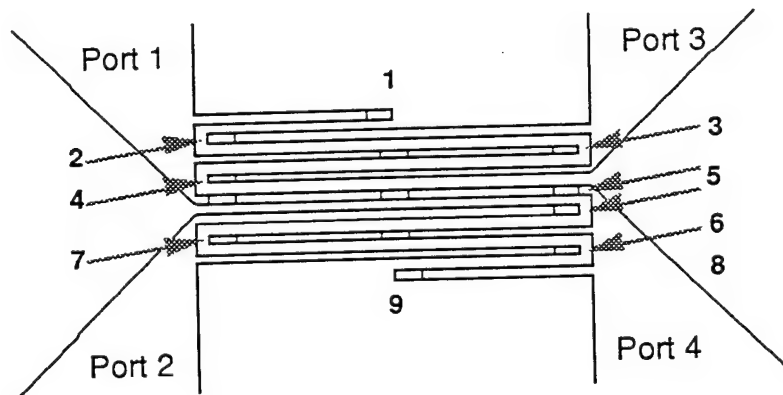


Figure 4-4. Enlarged View of HTS 8-Finger Lange Coupler.

In Figure 4-5, a photograph of the practice bonding area on the substrate die. A unique process improvement by the use of single wire bonding in the center region where typical processes needed several bonds. One .001" Au wire was stitch-bonded to the silver pads greatly increasing the yield during the bonding process.

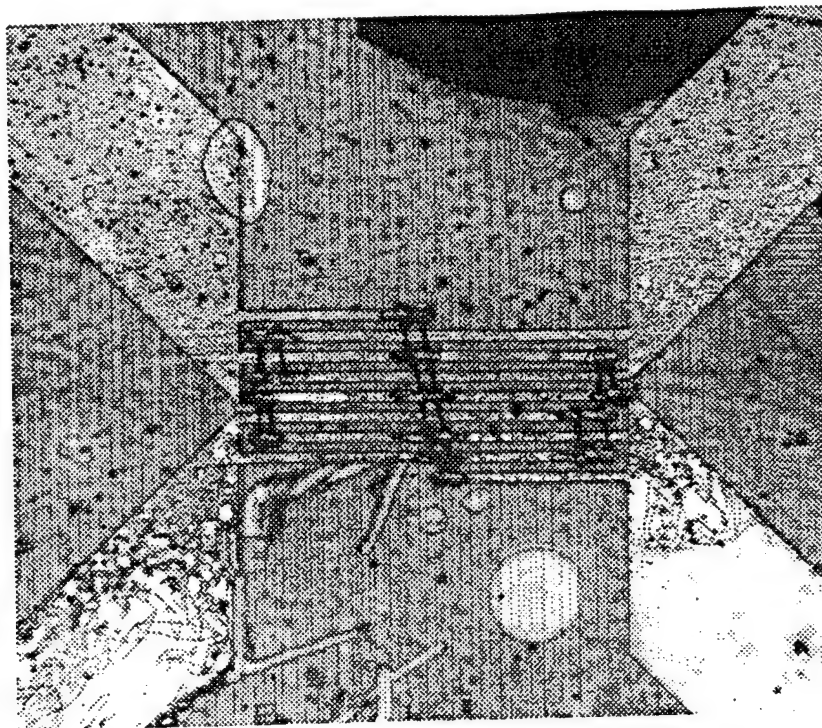


Figure 4-5. Photograph of the practice bonding area on the HTS Lange coupler chip.

The EESOF Touchstone program was used to analyze and design the coupler and transformer system. Figure 4-6 shows the coupling performance predicted for the HTS Lange coupler by this program.

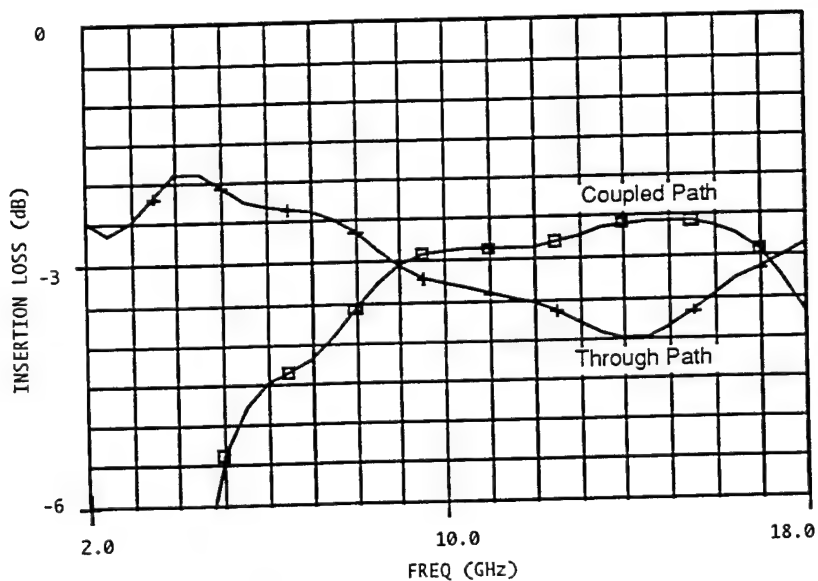


Figure 4-6 Predicted HTS Coupler Performance.

Figure 4-7 shows the measured insertion loss results of the HTS experimental Lange couplers and the results for a reference Ag (silver) coupler, fabricated to indicate performance of a cooled non-superconductor circuit. The insertion loss improvement over the band is approximately 0.5 to 1 dB across the usable band of the coupler. The ripple in the pass band is caused by test set calibration effects and design of the transformer.

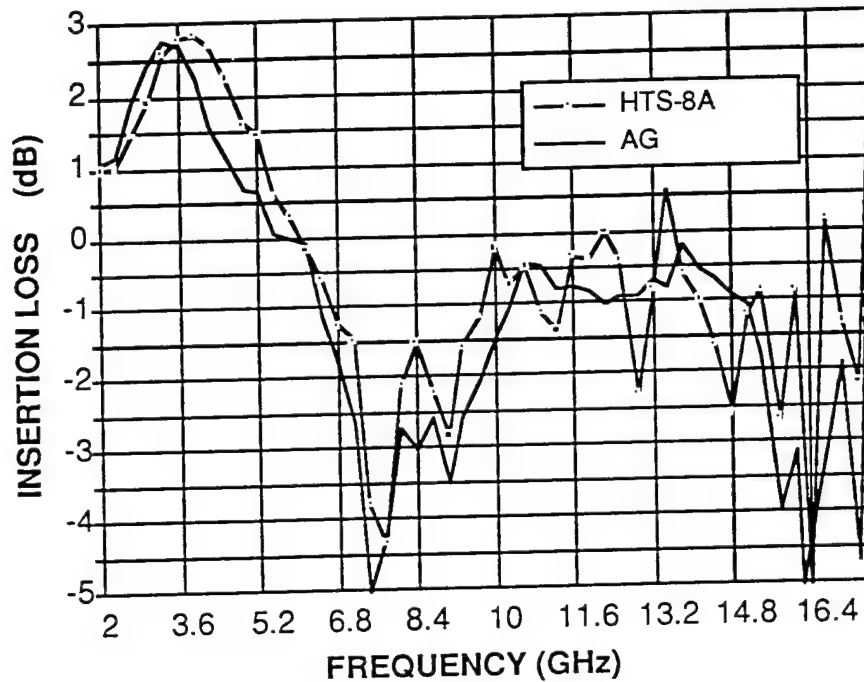


Figure 4-7. Measured HTS Coupler and Ag Coupler Performance at 77K.

The Lange coupler design uses a transformer in cascade with the coupler so that the coupler design uses a lower impedance that allows physically realizable line widths to be used; however, the design of the transformer was band-limited due to the high dielectric properties of LaAlO_3 . This band limiting occurs when the quarter-wave section aspect ratio is close to that of a radiating patch antenna.

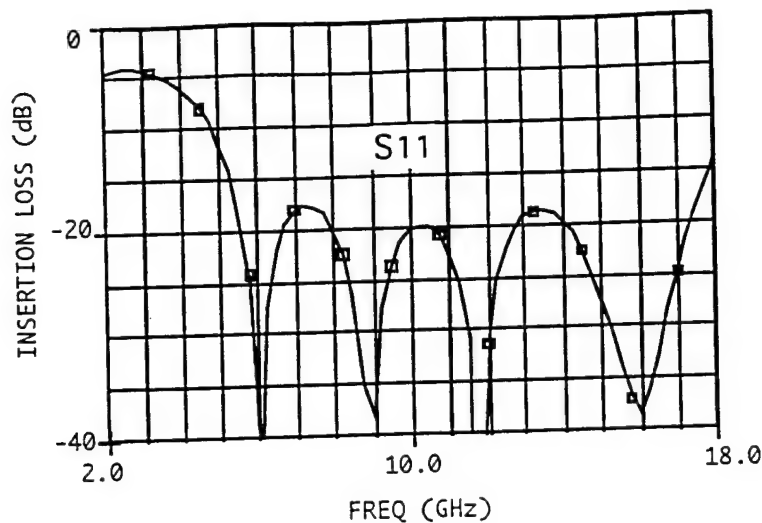


Figure 4-8. Theoretical Return Loss of Back-to-Back Transformers.

A calculation of the theoretical return loss of the back-to-back transformer circuit is shown in Figure 4-8. The 1.2:1 VSWR bandwidth of the circuit is 5 to 17 GHz. The Touchstone analysis of this circuit does not take into account the effects of radiation from the resonant patch elements. This radiation effectively reduces the performance of the transformer as shown in Figure 4-8. In addition, the 0.020" thickness of the dielectric substrate, chosen to give a reasonable finger line width and spacing for the device characteristic impedance of 18Ω , is nearly $1/8$ wavelength at 18 GHz and allows a non-TEM propagation mode.

The measured return loss of two transformers that are cascaded back-to-back is approximately 10 dB from 5-13 GHz and is shown in Figure 4-9. This return loss differs from theoretical prediction due to standard microwave microstrip launching techniques effects. These launcher techniques were studied and multiple ribbon interfaces on each microstrip launcher offered the best performance since they reduced stray lead inductance.

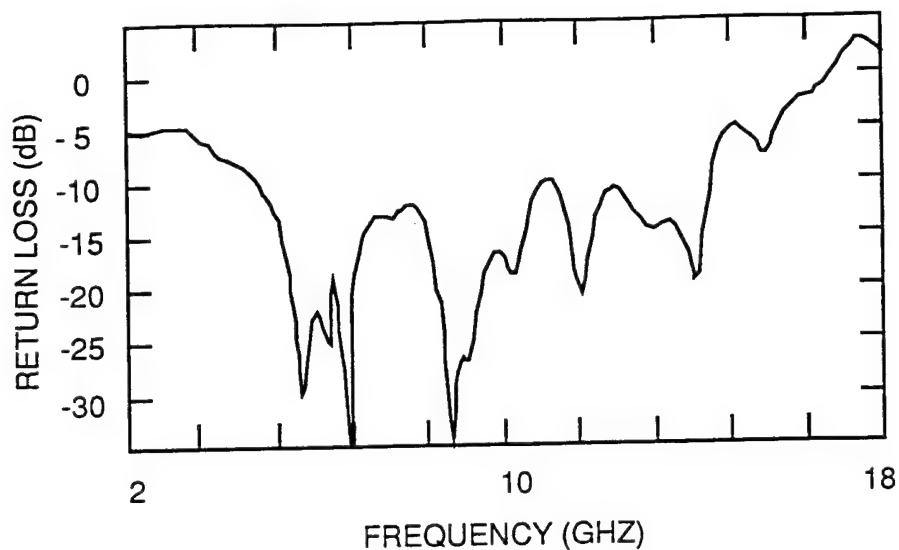


Figure 4-9. Measured Return Loss of Back-to-Back Transformers.

A major shortcoming of the Lange coupler design and fabrication was the failure to meet the impedance level goal. The design of the transformer was analyzed and optimized to meet this goal; however, as shown in Figure 4-10, the time domain reflectometer measurement of two back-to-back transformers indicates that the impedance is approximately $25\ \Omega$, compared to the $18\ \Omega$ design.

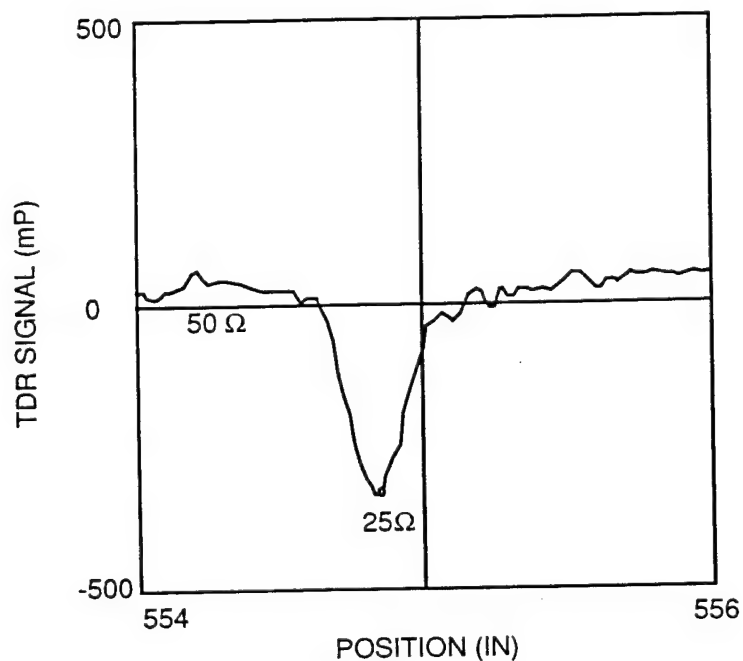


Figure 4-10 TDR of Lange/Transformer Circuit.

Figure 4-11 shows the TDR plot of the coupler/transformer circuit. This plot shows (see the central part of the curve) a change in impedance level that would indicate the Lange coupler's impedance and transformer's characteristic impedance are not the same.

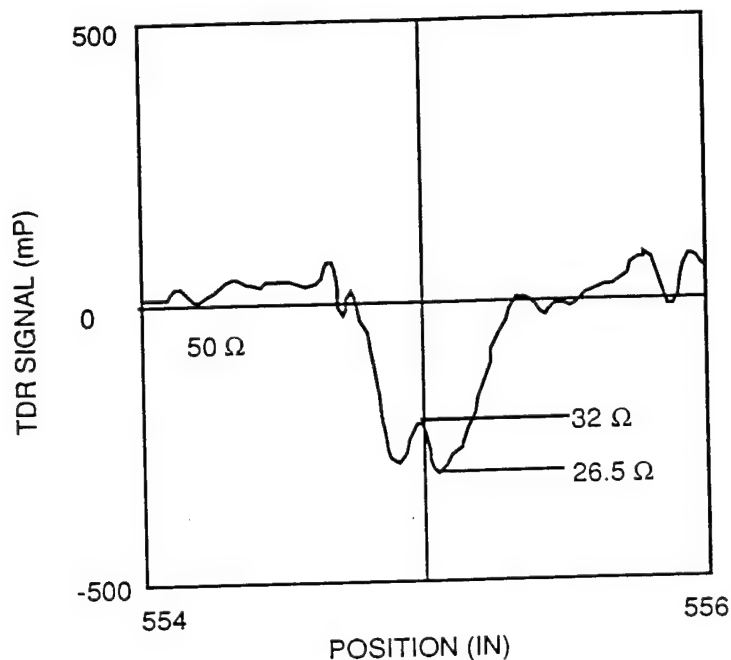


Figure 4-11. TDR of Back-to-Back Transformers.

Analysis was performed by a finite-element modeling program, EM Sonnet, on the geometry of a six-finger Lange coupler on LaAlO_3 and the results compared to the predicted performance using EESOF Touchstone's model of the same coupler. A comparison of the Touchstone s-parameters to the EM Sonnet values, Figure 4-12, shows that the s-parameters of the measurements are within a 2 dB window. This proves that the model used to design the HTS Lange is adequate when compared to the full-wave or FEM modeling tools. In this case the problem in the device's impedance level could be explained by a variance of the substrate material dielectric properties. A small difference in these dielectric properties could adversely affect the performance of the Lange coupler and transformer. In addition, the transformer's performance was limited by its resonant radiation.

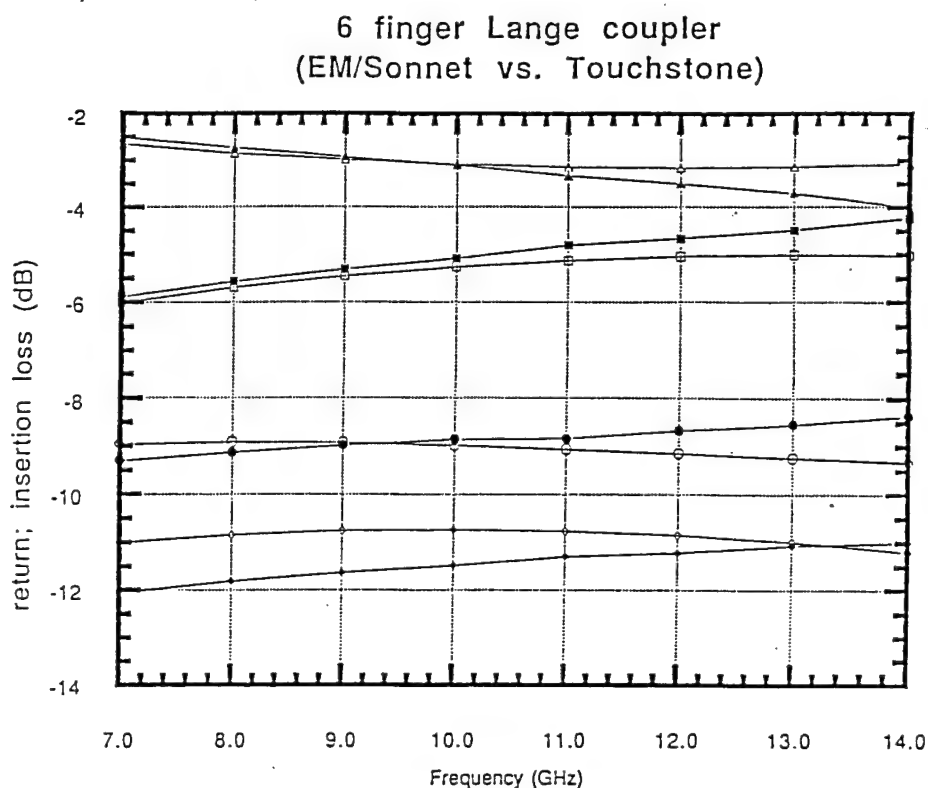
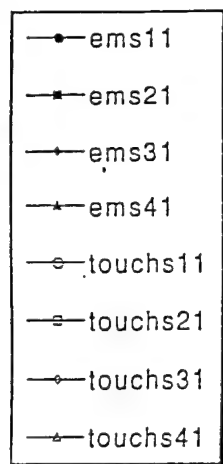


Figure 4-12. Full Wave Analysis vs. Circuit Model of 6-Finger Lange Coupler.

Future tasks should include an in-depth study of hybrid designs such as the microstrip/Lange coupler circuit. This circuit would model the interdigitated section of the Lange coupler as a lumped even-mode impedance and synthesize an even-mode distribution of microstrip coupled elements for a 10:1 bandwidth 3 dB coupler. Use of high resolution e-beam masks, offering fine line resolution of at least 1 μm would enable the design of Lange couplers with impedance levels of 50 ohms and not require the use of transformers. Microstrip design does not typically require such precise masks, while MMIC circuit design must these masks.

In future designs for high frequency devices, the thickness of the LaAlO_3 substrate should be limited to 0.010" to preclude frequency cutoff at Ku band due to non-TEM modes of propagation. Data should be taken and analyzed for anisotropic properties of the LaAlO_3 substrate material. Possible degradations seen in the performance of the coupler could indicate that material repeatability could be a factor. An improvement in launching techniques would be advantageous to all microwave circuit evaluation in the future. Included with any additional tasks should be an finite-element

analysis of the circuit to include radiated losses and other deleterious affects. Tools such MSC-EMAS, Sonnet, or Ansoft's Maxwell should be utilized for maximum risk reduction in designing microwave circuits on high dielectric constant material.

4.2 Broadband HTS Power Divider/Combiner Design and Test

A Wilkinson power divider is a common RF circuit that is the basis of many beamforming networks. It offers a wide operational bandwidth that is relatively easy to implement. The isolation between output ports is achieved by cancellation of the reflected waves through the dissipation of the residual energy in a termination resistor. The resistor material that was chosen for the HTS Wilkinson device was NbN (niobium nitride.) The material was considered a good candidate due to the low contact resistance between it and the Ag contact pads. The circuit schematic of the Wilkinson power divider is shown in Figure 4-13. Values of the junction resistors and widths of the high impedance lines were calculated to determine the input impedance of the splitter. The resistor aspect ratio was calculated based on the NBN resistivity, approximately 50 ohms/square for a 50 nm thickness, and the size of the pad area where the resistor would be deposited. For example, to get the resistance of 100 ohms, the aspect ratio of the NbN resistor, or w/h ratio, has to be 2:1.

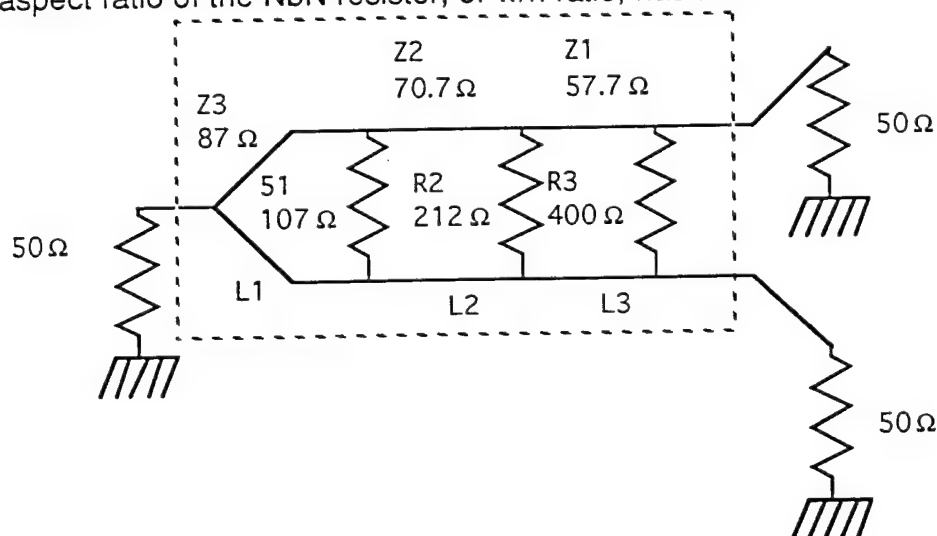


Figure 4-13. Schematic of Wilkinson Power Divider.

Table 4-4 shows the characteristic impedance of the Wilkinson power divider and the aspect ratios of the junction resistors. In general, the aspect ratio must be greater than one. For a 50 ohm system, that condition is met by all junction resistor values. It was recommended that a Wilkinson power divider be designed and fabricated for a 50 ohm system.

System z=		50	40	30	25	20	10
Wilkinson normalized impedance							
z0=	1	50	40	30	25	20	10
z1=	1.1497	57.485	45.988	34.491	28.7425	22.994	11.497
z2=	1.414	70.7	56.56	42.42	35.35	28.28	14.14
z3=	1.7397	86.985	69.588	52.191	43.4925	34.794	17.397
r1=	8	400	320	240	200	160	80
r2=	4.229	211.45	169.16	126.87	105.725	84.58	42.29
r3=	2.14	107	85.6	64.2	53.5	42.8	21.4
resistor ohms/square	50	50	50	50	50	50	50
aspect ratio	must be greater or equal to one						
r1=		8	6.4	4.8	4	3.2	1.6
r2=		4.229	3.3832	2.5374	2.1145	1.6916	0.8458
r3=		2.14	1.712	1.284	1.07	0.856	0.428
r4=							

Table 4-4. Wilkinson Characteristic Impedance and Junction Resistor Aspect Ratios.

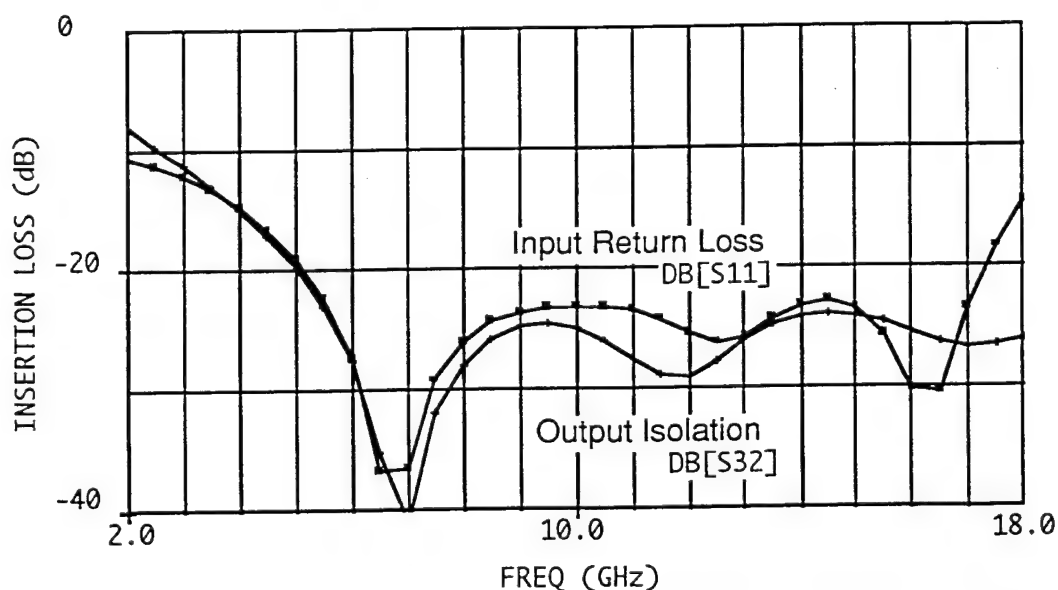


Figure 4-14. Theoretical Return Loss and Output Isolation of Wilkinson Device.

Figure 4-14 shows the theoretical return loss and output isolation of the HTS Wilkinson power divider. All RF analysis was performed using a PC-based EESOF Touchstone

linear analysis program. The theoretical output power coupling for the two outputs of the Wilkinson power divider is shown in Figure 4-15.

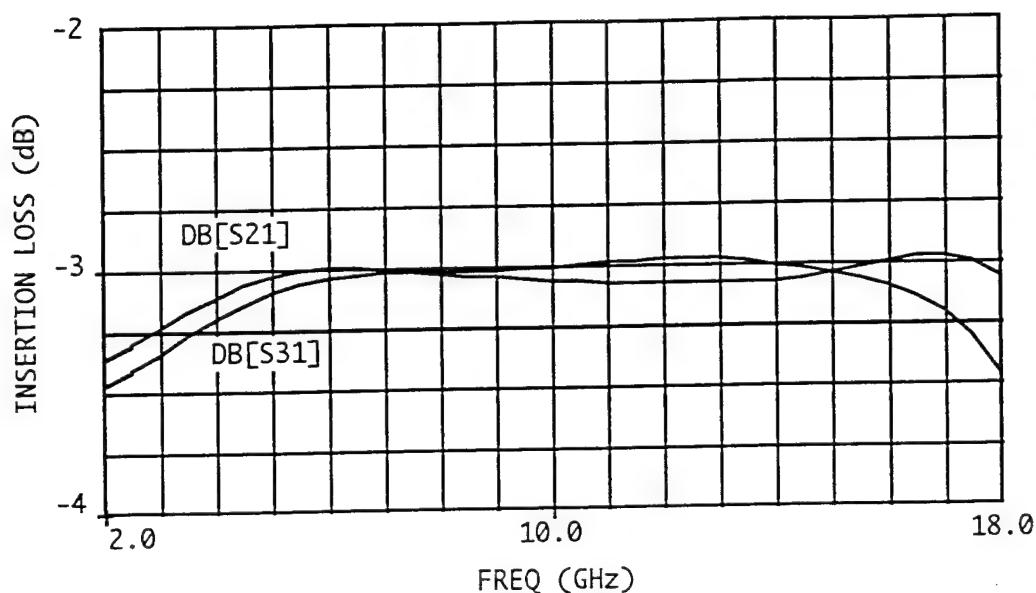


Figure 4-15. Theoretical Power Split Between Outputs of Wilkinson.

several observations were made during the testing stage of the HTS Wilkinson power dividers. The first was that the fabrication of the high impedance lines nearest the input was suspect. The lines were approximately 0.0002" (5 microns) in width. This is attributed to the resolution of the mask, based on a photographic process, as opposed to an e-beam mask. Of the four configurations that were fabricated only one worked. Of the three configurations that failed, all three devices were due to an open lines in the area where the highest impedance line (narrowest line) was fabricated. In Figure 4-16, the measured return loss of the PD-1 power divider is shown. The return loss indicates a 2:1 VSWR over a large portion of the band. One limitation on this measured performance was the microstrip launchers and the calibration process.

Figure 4-17 shows the measured insertion loss including the coupling loss for one of the Wilkinson Divider output ports. The operational bandwidth of the device is approximately 2 to 14 GHz. At about 10 GHz, a large "suckout" occurs in the passband due to a non-TEM mode of propagation that causes a large interfering signal to be summed with the incident signal. The insertion loss, including the 3 dB splitting loss, is approximately a constant 1 dB up to 10 GHz. The isolation was also measured indicating a good connection between the ohmic contact and the resistive NbN and good uniformity in the aspect ratio providing the correct resistance value. It is

recommended that an Ag device of similar design be fabricated in any additional work to allow a comparative measurement.

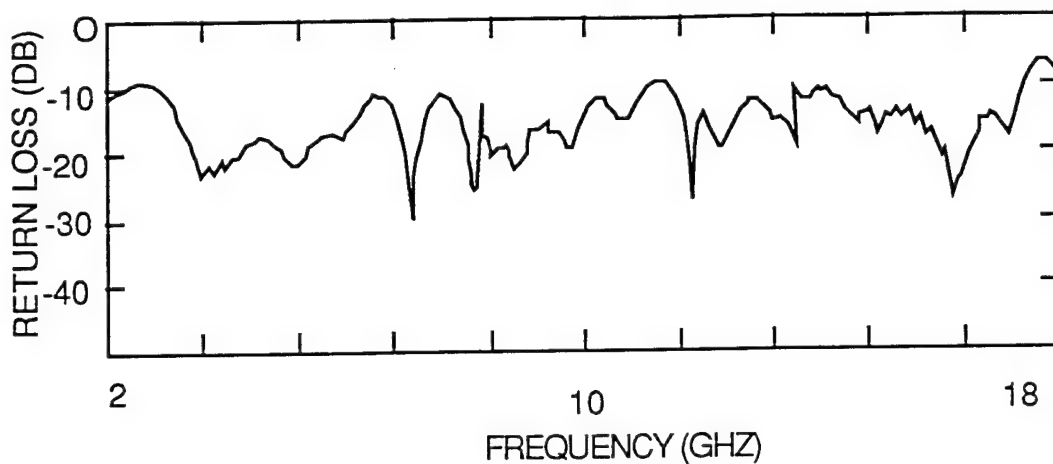


Figure 4-16. Measured Return Loss of HTS Wilkinson Power Divider.

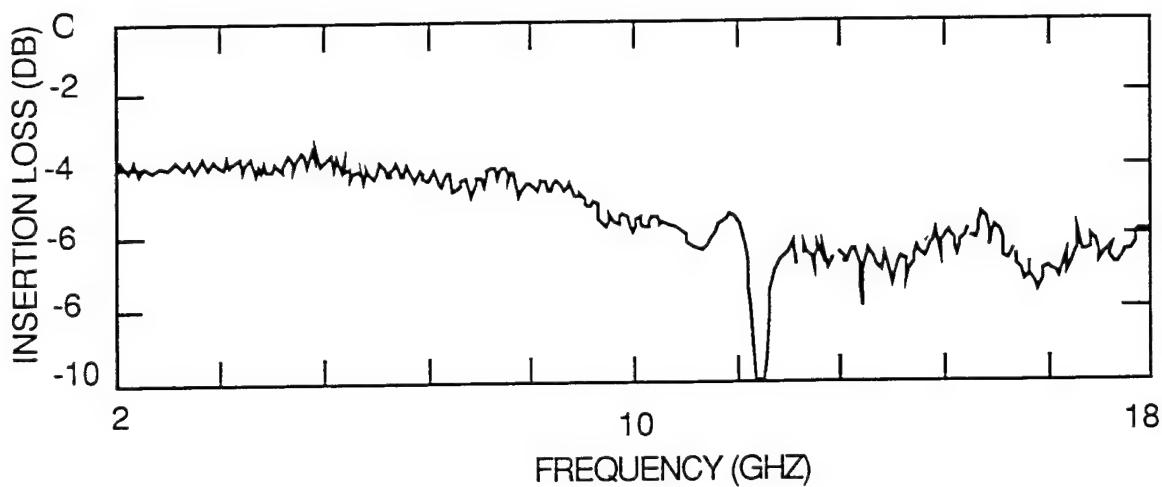


Figure 4-17. Measured Insertion Loss of HTS Wilkinson Power Divider

4.3 Monopulse Beam Forming Network

A monopulse network is a beam forming network (BFN) used for microwave applications. The term monopulse refers back to a time when the BFN was used in radar applications and "one pulse" contained all the information- range and pointing error correction. Today one of the principal applications is to allow a communication antenna to track the signal source without wobbling around. Another application uses the monopulse BFN for direction finding.

The purpose of this demonstration was to show that a number of components, such as those just described, could be integrated into a monolithic design while providing reduced loss compared to a normal metal BFN. The design was originally intended for use in a HTSSE payload, and a copy was delivered to NRL.

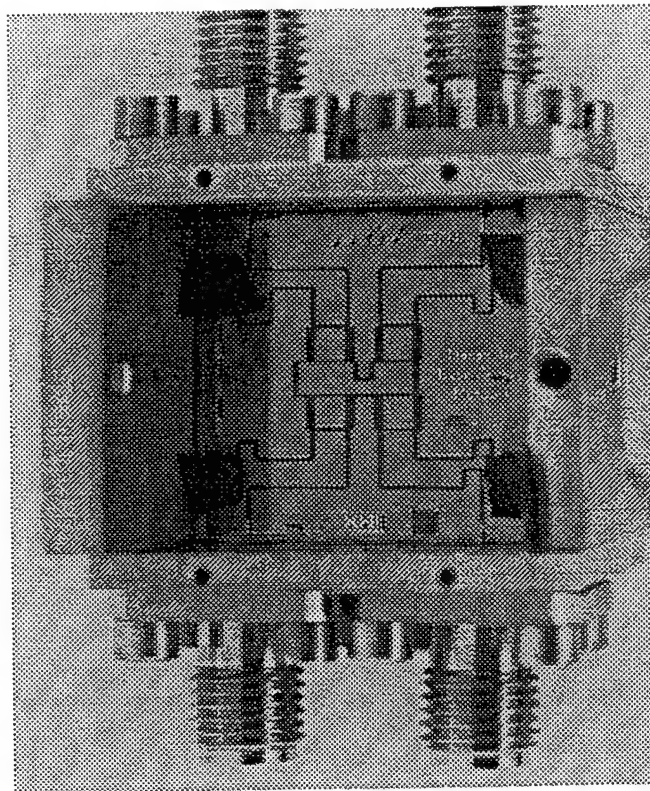


Figure 4-18. Photograph of the HTS monopulse beamforming network in a test fixture.

A monopulse network, Figure 4-18, consists of a number 180° hybrids, formed into a Butler array, Figure 4-19. A common way to make a 180° hybrid is to combine a 90° hybrid with a 90° fixed phase shifter on the input. The 90° hybrids are made with

either branchline or Lange configurations. For many applications, there is no need to develop a cross-over. For instance, the topology shown in Figure 4-20 can be used. The present design uses a branchline approach because the HTSSE communication demonstration did not require the broad bandwidth demonstrated in the previous designs. The fixed phase shifters are made with quarterwave length of line, or with Schiffman coupled line sections. The present design uses quarterwave lines.

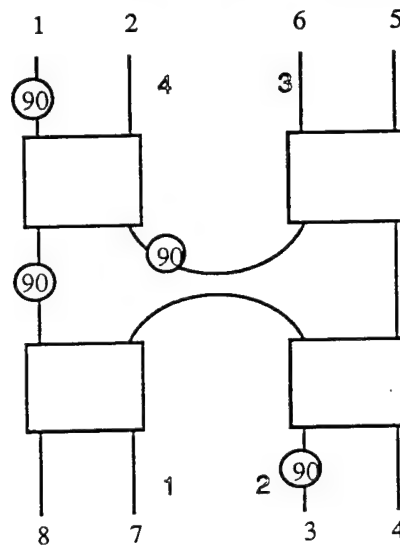
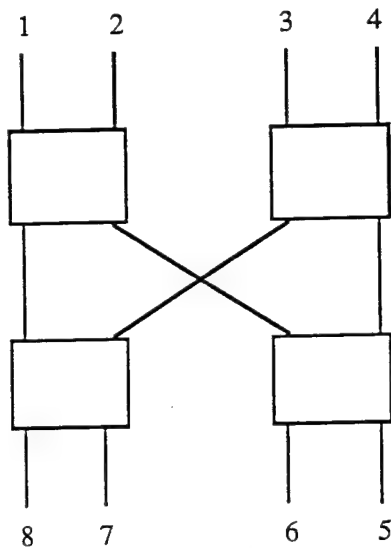


Figure 4-19. Standard monopulse layout with inputs on top and outputs on bottom. Figure 4-20. Modified monopulse layout without crossover.

The circuit layout should have the same length of lines between each input (antenna) and the detector. There are 4 inputs and 4 outputs on the 0.7"x0.7"x20-mil thick LaAlO_3 substrate with a silver ground plane. The line widths are determined from a table of impedance and effective dielectric constant.

TOUCHSTONE was used to calculate the monopulse BFN response shown in a plot of the insertion loss vs frequency shows that the ports are either isolated (with high insertion or return losses) or coupled (with 6 dB insertion losses). Figure 4-21 shows the calculated insertion loss and return loss for some of the ports.

Tables 4-5 and 6 summarize the data on an all silver circuit and for an HTS circuit on a silver ground plane. Both S_{12} and S_{32} have lower losses (comparing the Ag circuit with the HTS one), attributed to mismatch effects and internal reflections which are exacerbated by lower transmission line losses. Both S_{22} and S_{42} have smaller

magnitudes attributed to K-connector to microstrip mismatches, to 6-feet of input cables, and to poor microstrip terminations. Figures 4-22 and 23 show data on the HTS monopulse circuit.

In conclusion, the data in the tables show that there is more than a 2 dB improvement in performance for an HTS BFN compared to the Ag one. The responses do not correspond to the loss free calculation because the microstrip launchers and the microstrip loads were not optimal. In addition, 6-feet of cable to the cooled device made improved calibrations difficult to achieve.

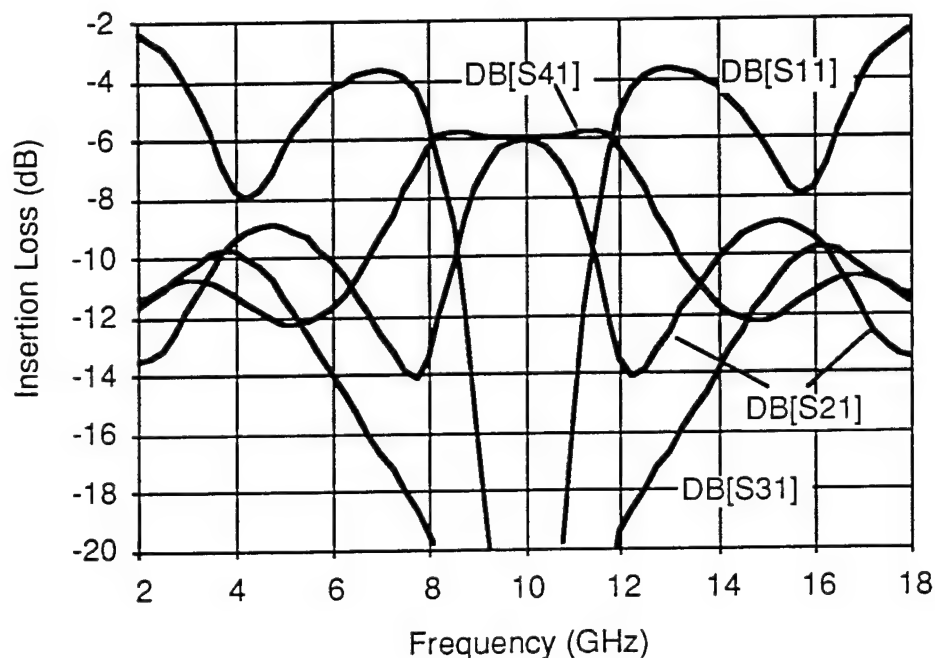


Figure 4-21. Insertion Loss vs frequency for the monopulse circuit. Note that S_{11} & $S_{31} < -20$ dB, while S_{21} & $S_{41} = -6$ dB. In general, the insertion loss is either 6dB, or it is greater than 20 dB at the center frequency. In all, for the 4 inputs and the 4 outputs, there are 36 responses to measure.

AG @ 9.5 GHz	Data (dB)	Loss Free Theory (dB)	HTS @ 10 GHz	Data (dB)	Loss Free Theory (dB)
S ₁₁	-20	-20	S ₁₂	-5.9	-6
S ₂₁	-10.7	-6.4	S ₂₂	-12.7	-20
S ₃₁	-15	-20	S ₃₂	-3.3	-6
S ₄₁	-8.2	-6	S ₄₂	-19.2	-20

Table 4-5. Ag transmission line on Ag ground. Both S₂₁ and S₄₁ have higher losses (compared to the HTS circuits, Table 4-6), attributed to ohmic losses. Both S₁₁ and S₃₁ have smaller magnitudes attributed to K-connector to microstrip mismatches, and to poor microstrip terminations.

Table 4-6. HTS transmission line on Ag ground plane. Both S₁₂ and S₃₂ have lower losses than Table 4-5. When the losses were smaller than expected, the effect is attributed to mismatch effects and internal reflections which are exacerbated by lower transmission line losses. S₂₂ and S₄₂ have smaller magnitudes attributed to 6-feet of input cables, in addition to the causes listed in Figure 4-5.

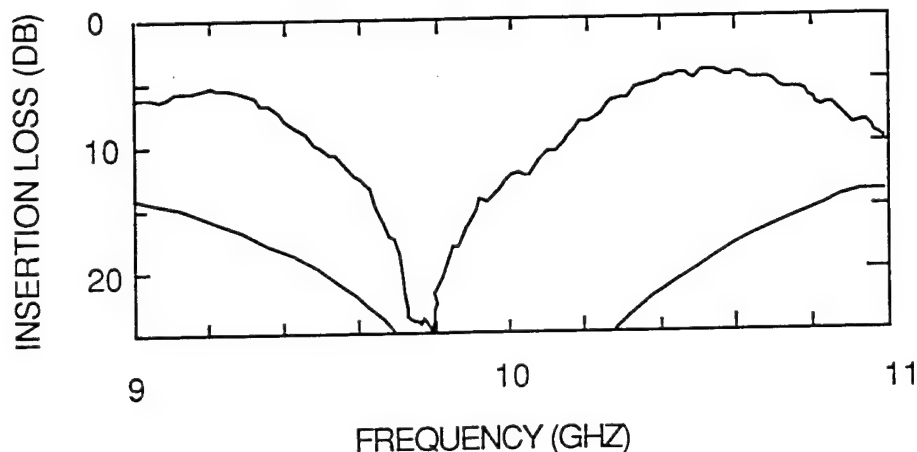


Figure 4-22. Measured insertion loss as a function of frequency for S₁₁, at 70 K for an HTS circuit over an Ag ground plane. The long cables used to hold the sample above a liquid Helium bath cause the ripples, and deviations from matched loads cause the shift in resonance for the return loss. The smooth line is the calculated response.

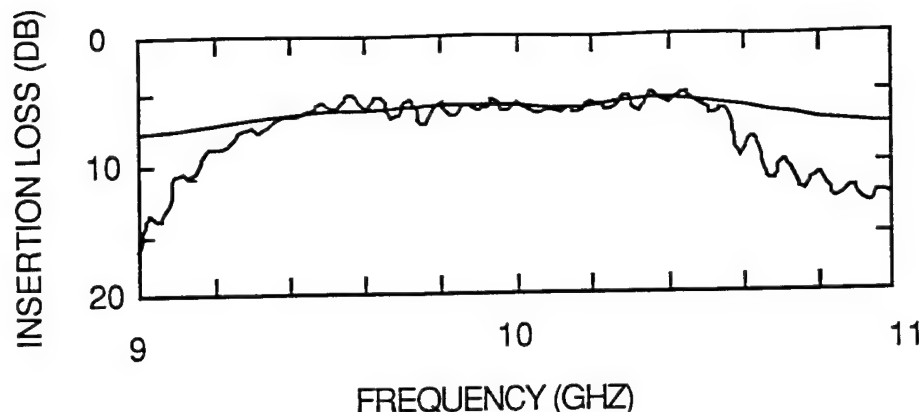


Figure 4-23. Measured insertion loss as a function of frequency for S_{41} , at 70 K for an HTS circuit over an Ag ground plane. The smooth line is the calculated response.

4.4 Design Considerations for an HTS/Ferroelectric Phase Shifter

The combination of HTS and ferroelectric materials offers a new approach to microwave phase control devices. These simulations show that the effect is surprisingly large. High temperature superconductor (HTS) phase shifters have been identified as a new device with potential impact on phased array systems. The combination of the low loss of HTS and the variable dielectric constant of ferroelectric materials for phase shifter applications has been explored for a number of years, but progress on these devices has been limited by lack of a suitable combination of materials. Fortunately, the lattice parameters of the ferroelectric material $\text{Sr}_x\text{Ba}_{1-x}\text{TiO}_3$ matches the high temperature superconductor $\text{YBa}_2\text{Cu}_3\text{O}_7$ (YBCO) allowing the formation of phase shifters and other devices, such as tunable resonators.

The HTS/ferroelectric phase shifter is a distributed device formed with a transmission line made using a material with a variable dielectric constant, shown by the simple circuit model in Figure 4.4-1. The actual implementation uses coplanar waveguide with HTS metallization for low losses, and BaSrTiO_3 films for the variable dielectric material. The center conductor of the CPW line is biased with respect to the ground planes, as shown in Figure 4.4-2. A working phase shifter is shown in test fixture in Figure 4.4-3.

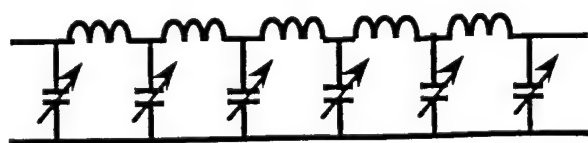


Figure 4.4-1. The HTS/ferroelectric phase shifter achieves phase shift changes by varying the capacitance per unit length.

Figure 4.4-1. The HTS/ferroelectric phase shifter achieves phase shift changes by varying the capacitance per unit length.

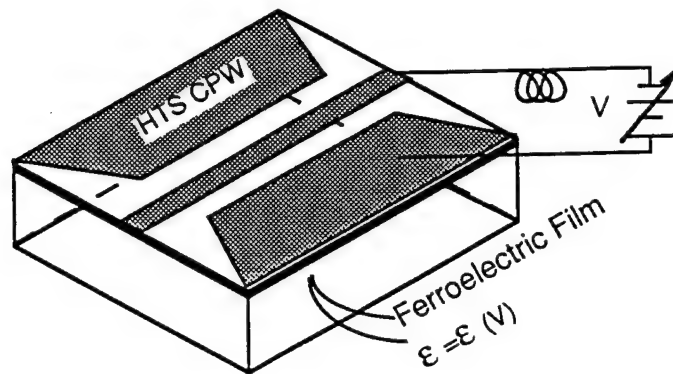


Figure 4.4-2. Schematic of the HTS/ferroelectric phase shifter showing how the ferroelectric film is biased.

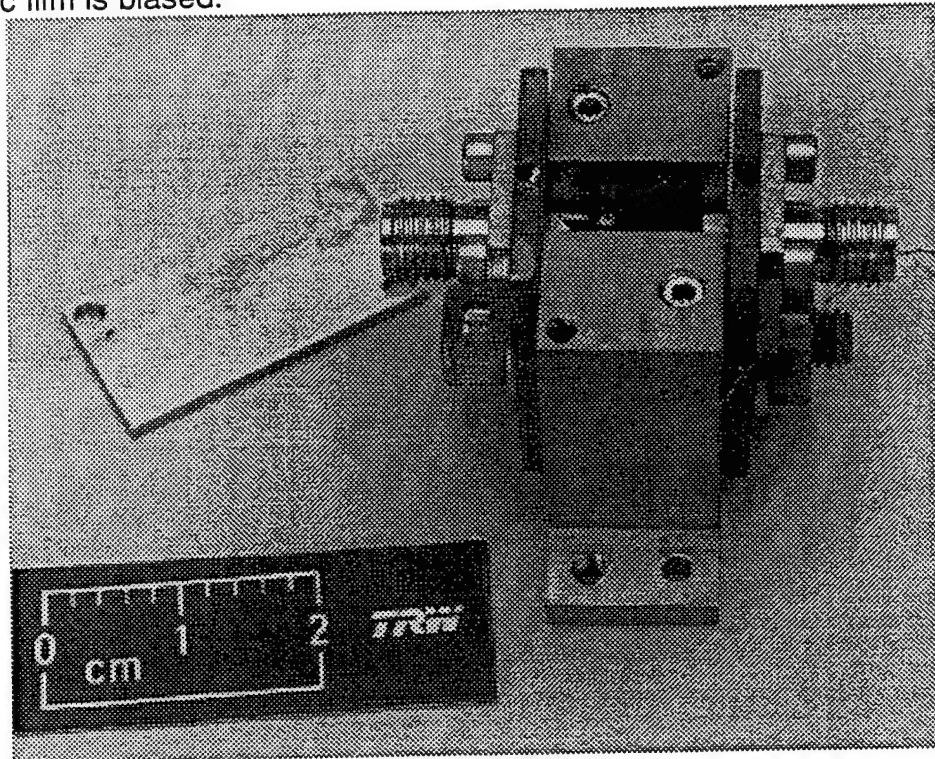


Figure 4.4-4 Photograph of an HTS/ferroelectric in a test fixture.

General Trade-offs

This section considers coplanar waveguide (CPW) geometries- earlier calculations have considered microstrip geometries, but the effects were not found to be as practical as the CPW geometry. In particular, a silicon substrate buffered with a $0.3 \mu\text{m}$

thick film of SrTiO_3 , and covered with a $0.3\text{ }\mu\text{m}$ thick layer of metallization is analyzed (Figure 4.4-4). The effect of a dc bias on the ferroelectric material was simulated by taking the maximum dielectric constant as 200 and the minimum value to be 100. The results are qualitatively similar to a LaAlO_3 substrate instead of the silicon one. The results are qualitatively similar to the case where the ferroelectric film is on top of the metallization.

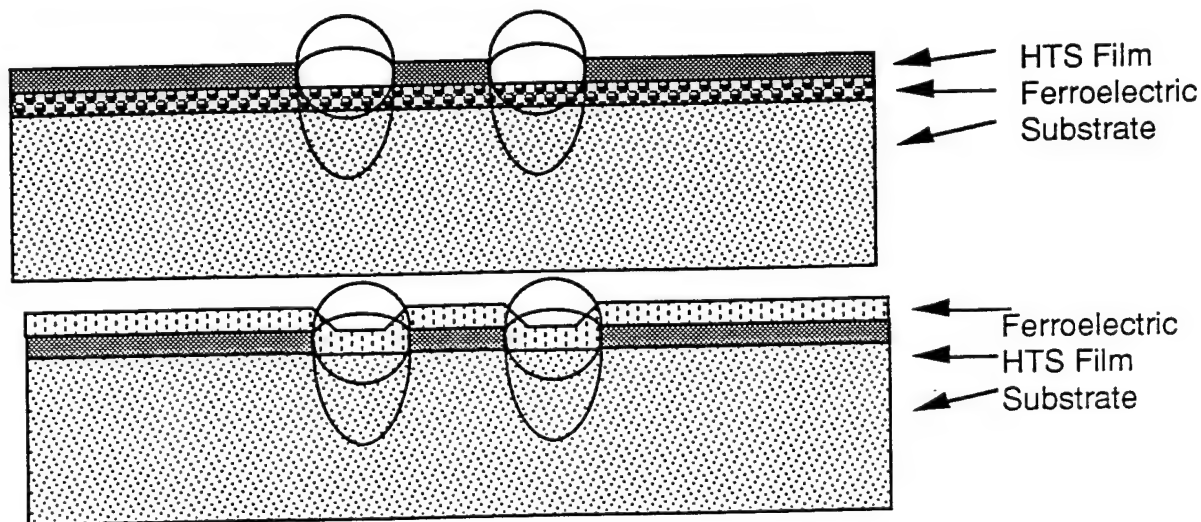


Figure 4.4-4 Coplanar waveguide (CPW) geometry, with thin buffer layer of HTS under the HTS transmission line and with the buffer film over the HTS films.

Some semi-quantitative results are interesting. A 1-cm line with a $2\text{ }\mu\text{m}$ wide center conductor and a $4\text{ }\mu\text{m}$ gap should allow a 150 degree phase change, with a 737 degree maximum phase delay. A total insertion loss of 1.4 dB is predicted for copper films, and an insertion loss of 0.014 dB is predicted for HTS lines. The predicted loss of the HTS line is so low that the dielectric loss of the ferroelectric film will dominate, with an insertion loss of 0.21 dB. For a $33\text{ }\mu\text{m}$ wide line, a smaller 15 degree phase shift per cm is expected.

Figures 4.4-5 and 6 show that the phase shift and the insertion loss are acceptable. Figure 4.4-7 shows that the power handling is limited by the HTS critical current carrying capacity, but that reasonable loads are possible. Simple text book formulas were used to obtain these results (mainly Gupta's book "Microstriplines and Slotlines" Aertech Press, an article in IEEE Microwave Theory and Techniques vol MTT 40, 1668-1672 (1992), and another article in Microwave and Guided Wave Letters vol. 2, 385-387 (1992). This calculation shows that there is a significant effect, and

subsequent simulations (Figures 4-16 and 17) show good comparison to a numerical simulation program Sonnet.

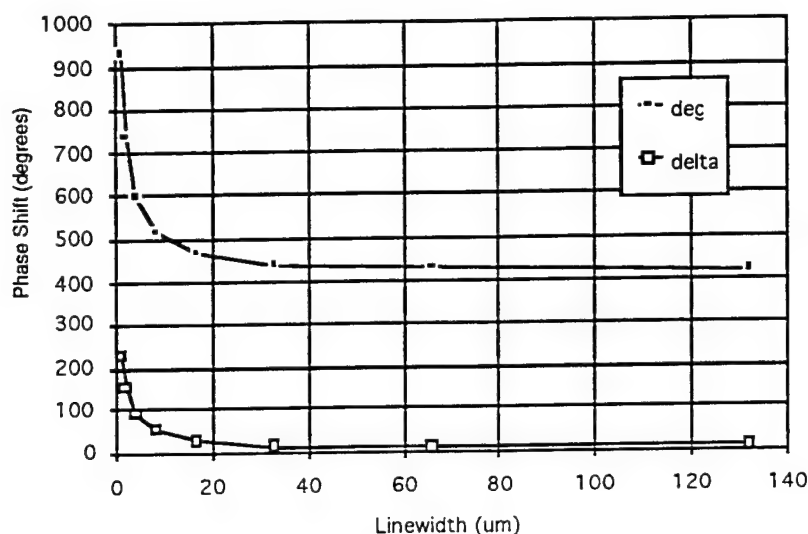


Figure 4.4-5. Phase shift vs linewidth. The upper curve shows the total phase shift at 10 GHz for a 1-cm long line. The lower curve shows the change in phase shift for a 1 cm long line when the buffer layer dielectric constant changes from 200 to 100 at 10 GHz.

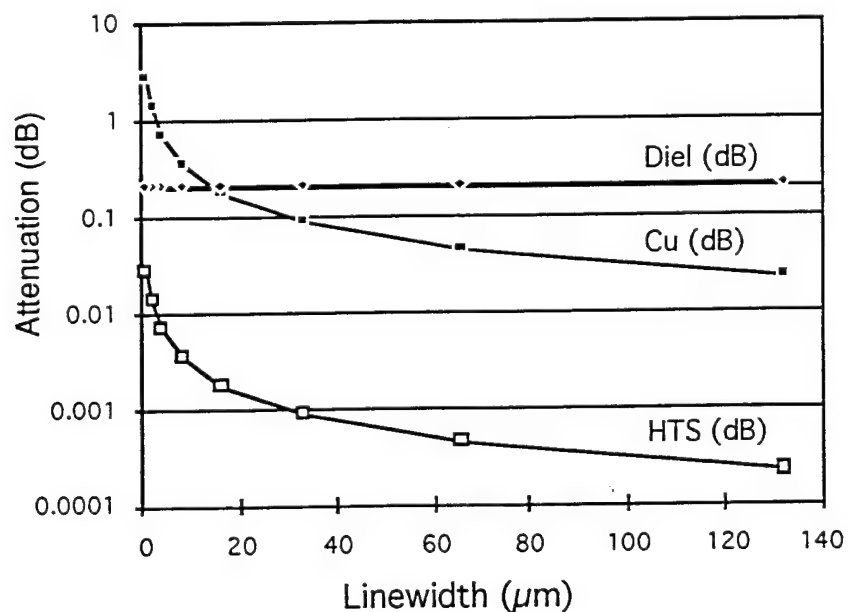


Figure 4.4-6. Attenuation vs linewidth. The upper curve A_{cu} shows the insertion loss at 10 GHz for a 1-cm long copper line. The lower curve A_{hts} shows the attenuation for a 1 cm long HTS line. The horizontal line A_{diel} shows the attenuation for a 1 cm long line with a loss tangent of 0.01. For copper, the loss is dominated by the ohmic losses

at very small lines and the dielectric losses at wide lines. The loss of the dielectric material exceeds the losses of the HTS line.

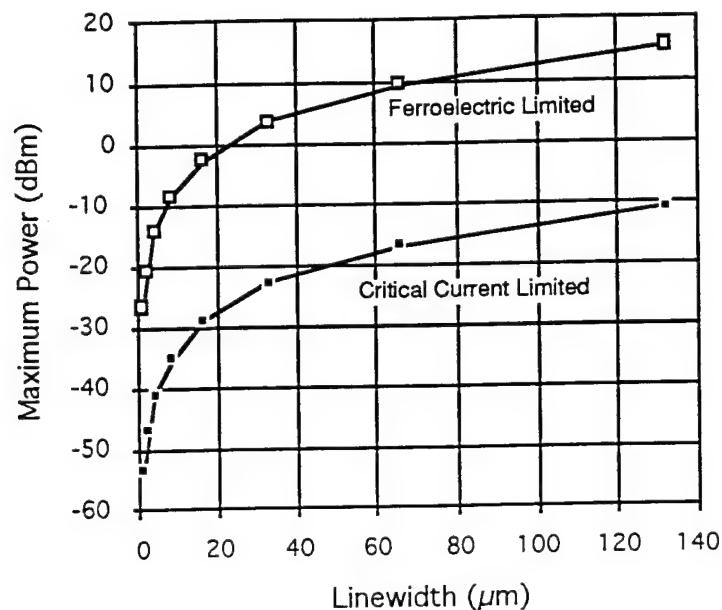


Figure 4.4-7. The Maximum power handling vs linewidth. Estimates of the maximum power handling limit for the CPW structures were based on two limits. The first case used the critical current as the limit: $P_c = I_c^2 Z$. The other case took the voltage along the line to be less than 1 kV/m (1 mV/μm), so $P_v = V^2/Z$.

Effective Dielectric Constant Calculations

The combination of HTS and ferroelectric materials offers a new approach to microwave phase control devices. This section considers coplanar waveguide (CPW) geometries with LaAlO_3 substrates, covered with HTS films and buffered with a different thickness films of SrTiO_3 (Figure 4.4-4). The effect of a dc bias on the ferroelectric material, and the effects of less than ideal materials was simulated by taking a range of dielectric constants.

A program was written to analyse the effects of multilayer CPW structures using an effective volume model. The model is primitive, easily programable, and suitable for a first-cut analysis of the geometry. Figure 4.4-8 shows a decrease in impedance with increasing film thickness and buffer dielectric constant. The effect is smaller for larger gaps. The plot, Figure 4.4-9, shows the change in the effective dielectric constant with buffer dielectric constant for three buffer thicknesses for a narrow line. The effect for thick films with high dielectric constants can be large. The next plot, Figure 4.4-10, shows the change in effective dielectric constant is smaller with larger line and gap

dimensions. The program breaks down for this larger gap, because the large angle approximations are not accurate, so the two thinner values are coincident. For this limit a more accurate program such as SONNET may be needed.

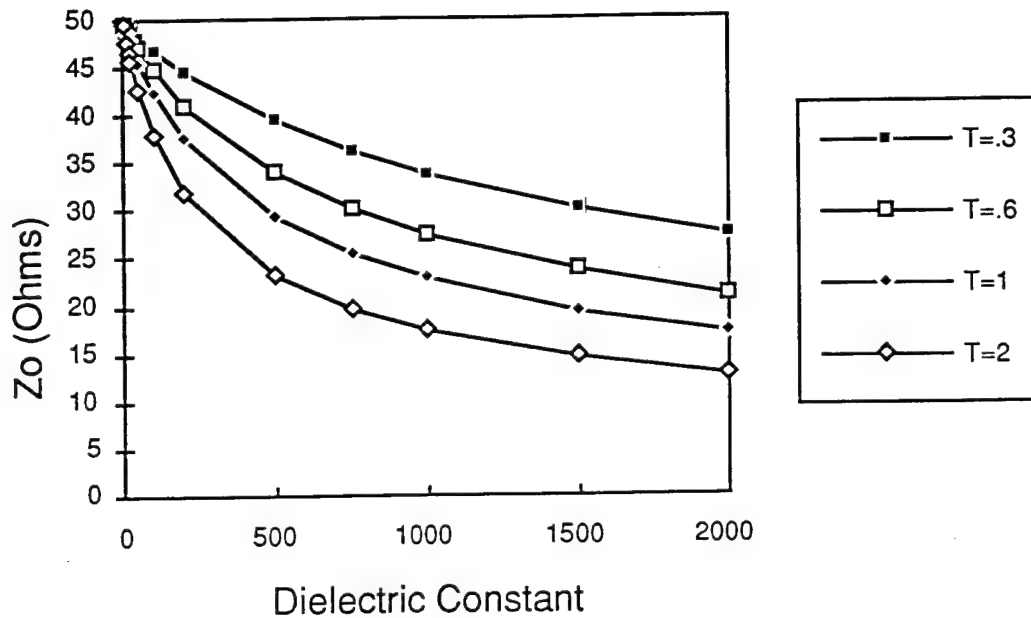


Figure 4.4-8. Effect of buffer dielectric constant and thickness on the characteristic impedance, for $S=10$ and $W=19 \mu\text{m}$.

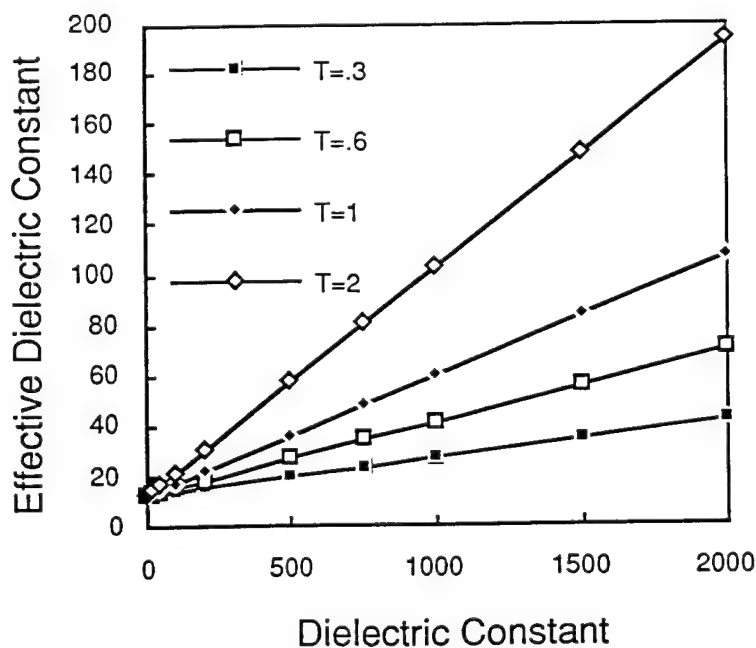


Figure 4.4-9. Relation of dielectric constant on effective dielectric constant for $S=10$ and $W=19 \mu\text{m}$.

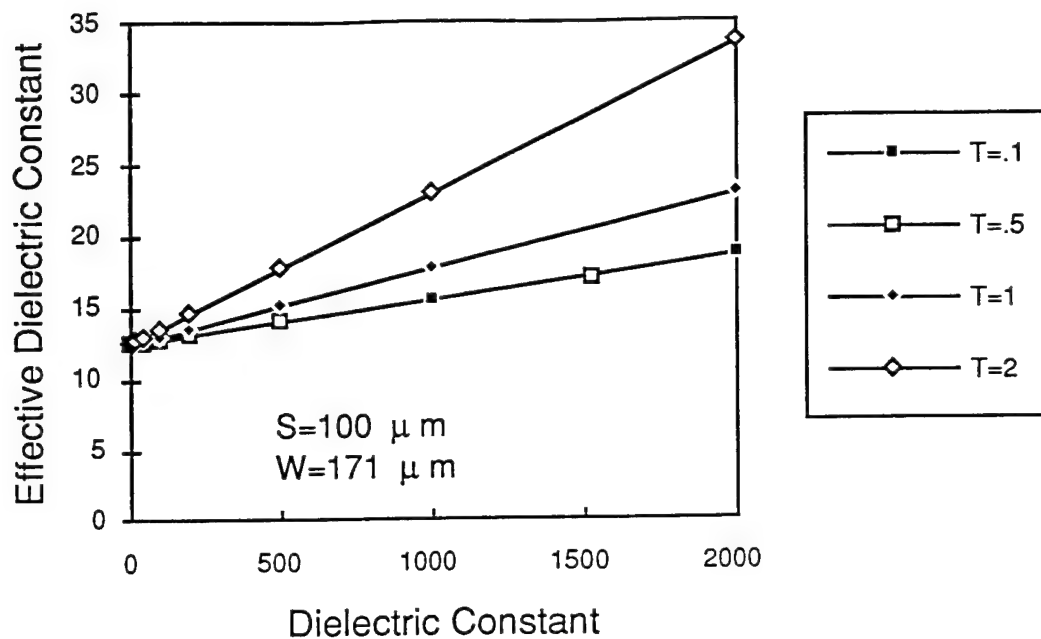


Figure 4.4-10. Relation of dielectric constant on effective dielectric constant for $S=100 \mu m$ and $W=171 \mu m$.

Effective loss tangent calculation

This section describes some effective loss tangent calculations performed on a multilayer CPW geometry, shown in Figure 4.4-4. The effective dielectric constant is calculated by a filling factor method, and comparisons to EM Sonnet show excellent agreement. The effective loss tangent can be obtained by this model, and it is compared to EM Sonnet simulations.

The dielectric constant of a material consists of a real and an imaginary part:

$$\epsilon = \epsilon' + i\epsilon'' \quad (1)$$

The loss in the material can be characterized by the loss tangent

$$\tan \delta = \frac{\epsilon''}{\epsilon'} \quad (2)$$

The definition of the loss tangent has been chosen for convenience; one reason is its relation to the Q of a resonator given by

$$\frac{1}{Q_o} = \tan \delta \quad (3)$$

For the multilayer structure considered here, an effective real part of the dielectric constant can be defined:

$$\epsilon'_{eff} = \sum_{i=1}^n q_i \epsilon'_i \quad (4)$$

Where q_i is the filling factor, and the subscript refers to the layer of the CPW structure. Similarly, an effective complex part can be defined:

$$\epsilon''_{eff} = \sum_{i=1}^n q_i \epsilon''_i \quad \text{or} \quad \epsilon''_{eff} = \sum_{i=1}^n q_i \epsilon'_i \tan \delta_i \quad (5 \text{ and } 6)$$

Consequently, an effective loss tangent can be defined as the ratio of the effective real and imaginary parts of the dielectric constant:

$$\tan \delta_{eff} = \frac{q_1 \epsilon_1 \tan \delta_1 + q_2 \epsilon_2 \tan \delta_2}{q_1 \epsilon_1 + q_2 \epsilon_2 + q_3 \epsilon_3} \quad (7)$$

where we have taken $\tan \delta_3 = 0$ for the layer of air above the ferroelectric film. The attenuation constant is related to the Q of a transmission line by

$$\alpha = \frac{27.3}{Q_o \lambda_m} \text{ (dB / cm)} \quad \text{where } \lambda_m = \lambda_0 / (\epsilon_{re})^{1/2} \quad (8)$$

For the case of microstrip and CPW this becomes

$$\alpha_d = 2.73 \frac{\epsilon_r}{\sqrt{\epsilon_{re}}} \frac{\epsilon_{re} - 1}{\epsilon_r - 1} \frac{\tan \delta}{\lambda_o} \text{ dB/unit length} \quad (9)$$

For the multilayer geometry, using the effective loss tangent definition, the expression is:

$$\alpha = \frac{0.91\sqrt{\epsilon}F(\text{GHz})}{Q_o}(\text{dB/cm}) \quad \text{or} \quad \alpha = 0.91\sqrt{\epsilon}F(\text{GHz})\tan\delta(\text{dB/cm}) \quad (10 \text{ and } 11)$$

Notes on the Quasistatic Calculation

The equations for the filling factors of the quasistatic calculation based on a conformal mapping analysis (J. Svacina, "A Simple Quasi-static Determination of Basic Parameters of Multilayer Microstrip and Coplanar Waveguide", IEEE Microwave and Guided Wave Letters, Vol. 2, pp 385-387 (1992)) are given below.

$$k_{i1} = \frac{\sinh\left(\frac{\pi}{4} \cdot \frac{s}{h_i}\right)}{\sinh\left[\frac{\pi}{4h_i}(s + 2W_1)\right]} \quad (12)$$

where s is the center line width, W_1 is the gap width, and h_i is the layer thickness. To calculate the filling factor, it is useful to define

$$k = k_{N+1} = k_{M+1} \quad (13)$$

The filling factor is given by

$$q_i = \frac{K'(k)}{2K(k)} \cdot \left[\frac{K(k_i)}{K'(k_i)} - \frac{K(k_{i-1})}{K'(k_{i-1})} \right] \quad (14)$$

Using this definition for the filling factor, it is possible to determine the effective dielectric constant

$$\epsilon_{eff} = \sum_{i=1}^{M+1} \epsilon_{ri}^l \cdot q_i + \sum_{j=1}^{N+1} \epsilon_{rj}^l \cdot q_j \quad (15)$$

A similar definition was used above to determine the effective loss tangent.

For a CPW geometry, a series of plots can be generated for the total attenuation for a 1-cm length of line at 10 GHz. Figure 4.4-11 shows attenuation values for different real parts of the dielectric constant, for different values of the film loss tangent, for a 0.3 μm thick film on a 508 μm LaAlO₃ substrate with a 10 μm wide line and a 19 μm gap. Figure 4.4-12 is the same data, but in a 3-D perspective.

The next set of figure 4.4-13 through 15 shows the effective loss tangent versus film dielectric constants for different film loss tangents. The thicker films have higher loss

tangents. Figure 4.4-13 was calculated with the quasistatic analysis, while 4.4-14 and 15 used EM Sonnet.

A comparison of the effective dielectric constants (Figure 4.4-16) and the effective loss tangents (Figure 4.4-17) as calculated by SONNET and the quasistatic model shows that the quasistatic model is surprisingly accurate.

Figure 4.4-18 shows the frequency dependence of the effective loss tangent as calculated by SONNET. The slight frequency dependence may be due to the chosen length of line, or the cell size. Figures 4.4-19 and 20 show a roll-off of the effective dielectric constant for thicker films, for different film dielectric constants.

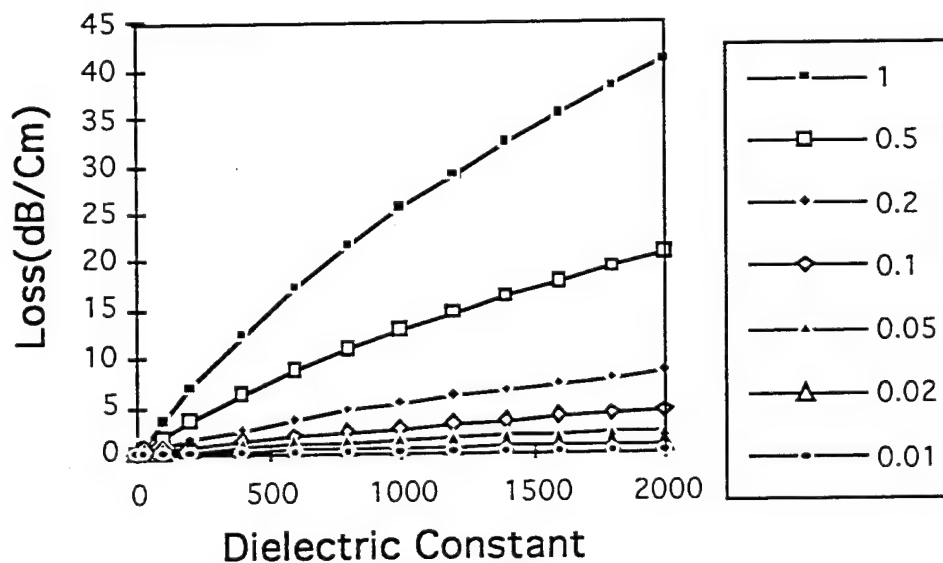


Figure 4.4-11. Plot of attenuation versus film dielectric constant for different film loss tangents at 10 GHz. Based on a quasistatic calculation for $s=10 \mu\text{m}$, $w=19 \mu\text{m}$, and $t=0.3 \mu\text{m}$.

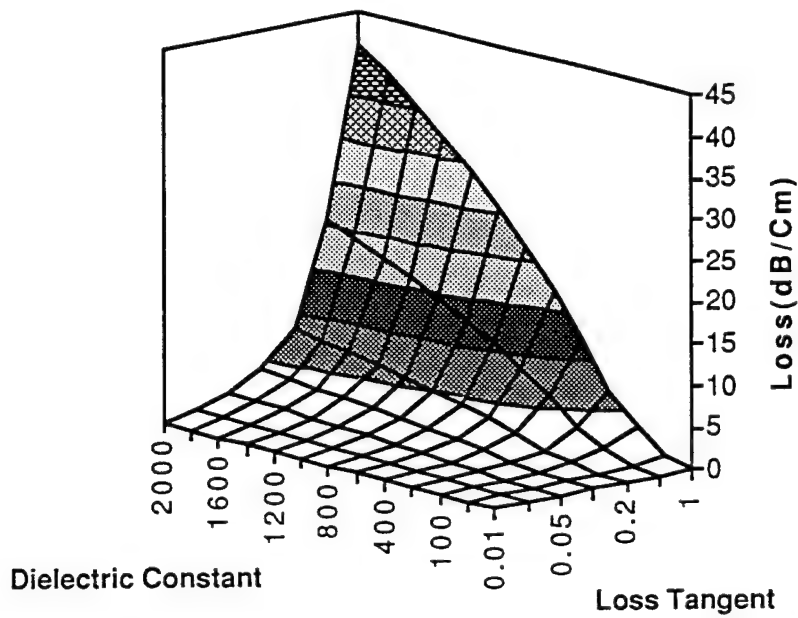


Figure 4.4-12. 3-D plot of attenuation for different film dielectric constant and film loss tangents at 10 GHz. For $s=10\text{ }\mu\text{m}$, $w=19\text{ }\mu\text{m}$, and $t=0.3\text{ }\mu\text{m}$. Based on a quasistatic calculation.

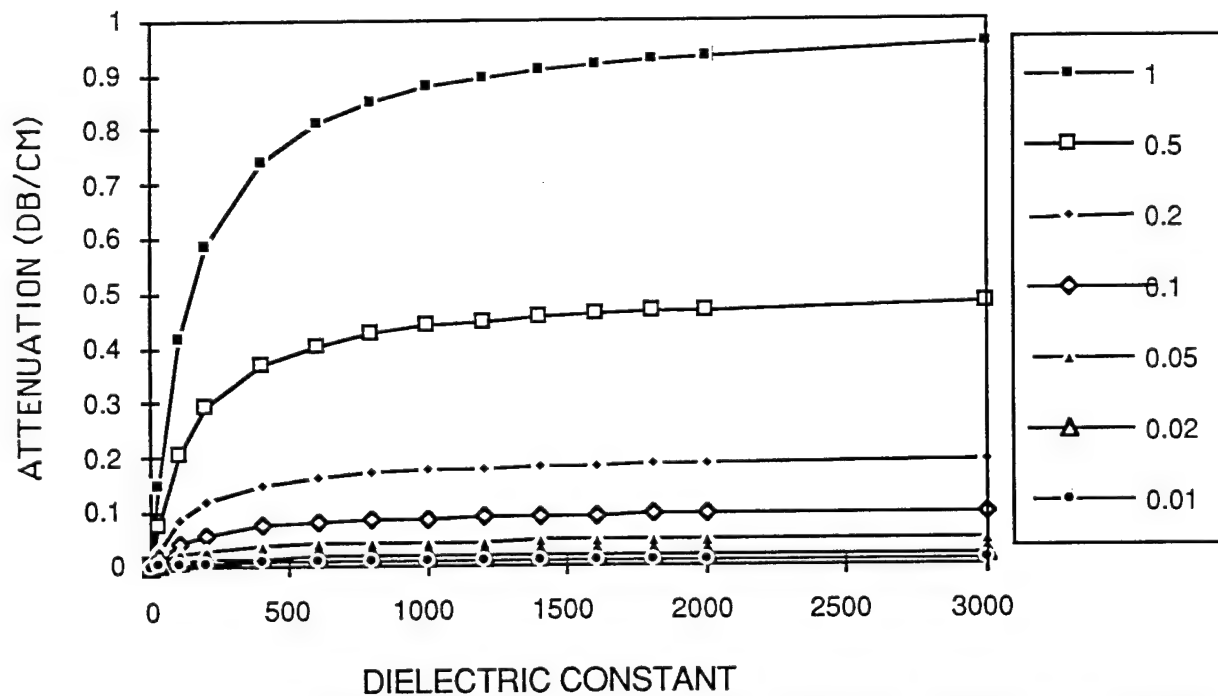


Figure 4.4-13. Plot of effective loss tangent versus film dielectric constants for different film loss tangents. For $s=10\text{ }\mu\text{m}$, $w=19\text{ }\mu\text{m}$, and $t=2.0\text{ }\mu\text{m}$. Based on a quasistatic calculation.

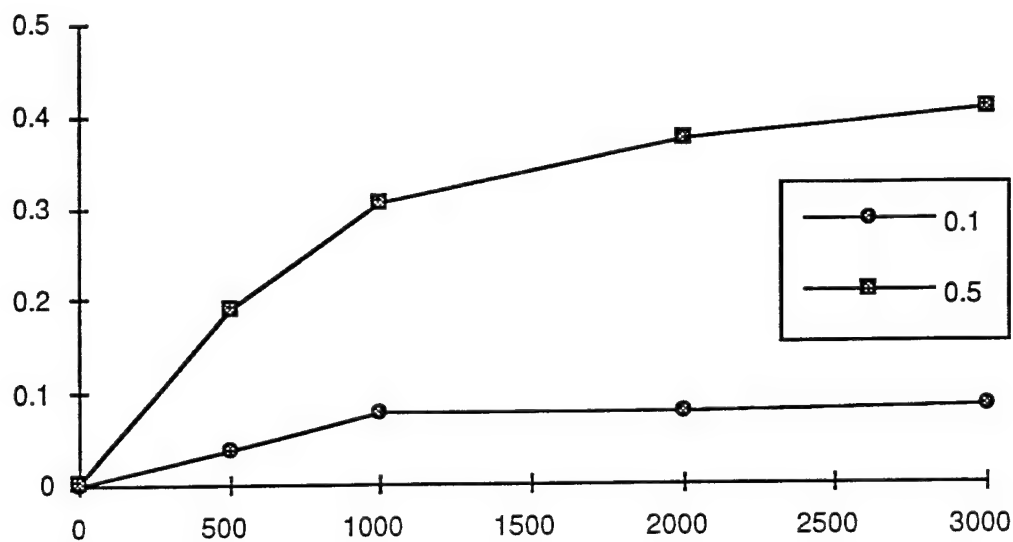


Figure 4.4-14. Plot of effective loss tangent versus film dielectric constants for different film loss tangents. Based on a SONNET calculation at 20 GHz for $s=10\text{ }\mu\text{m}$, $w=19\text{ }\mu\text{m}$, and $t=0.3\text{ }\mu\text{m}$.

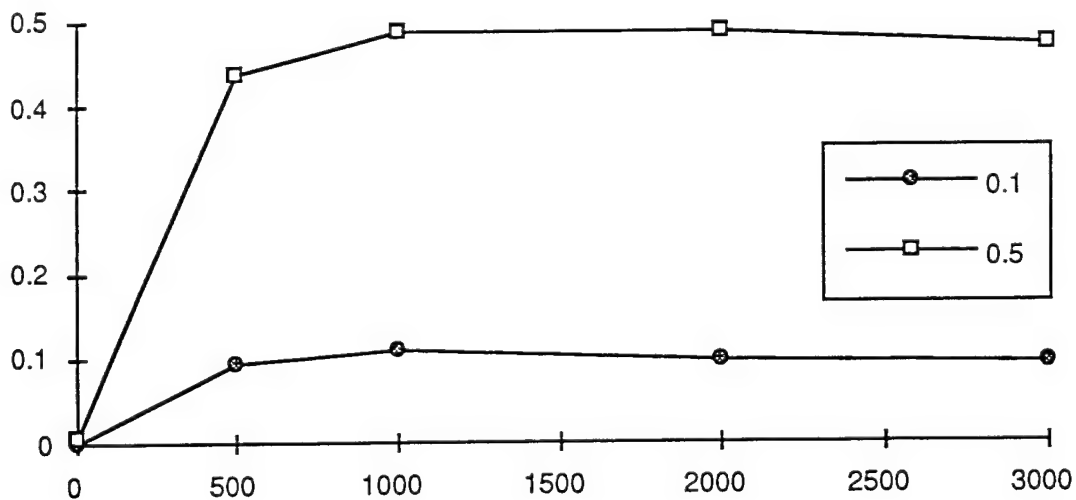


Figure 4.4-15. Plot of effective loss tangent versus film dielectric constants for different film loss tangents. Based on a SONNET calculation at 15 GHz for $s=10\text{ }\mu\text{m}$, $w=19\text{ }\mu\text{m}$, and $t=2.0\text{ }\mu\text{m}$.

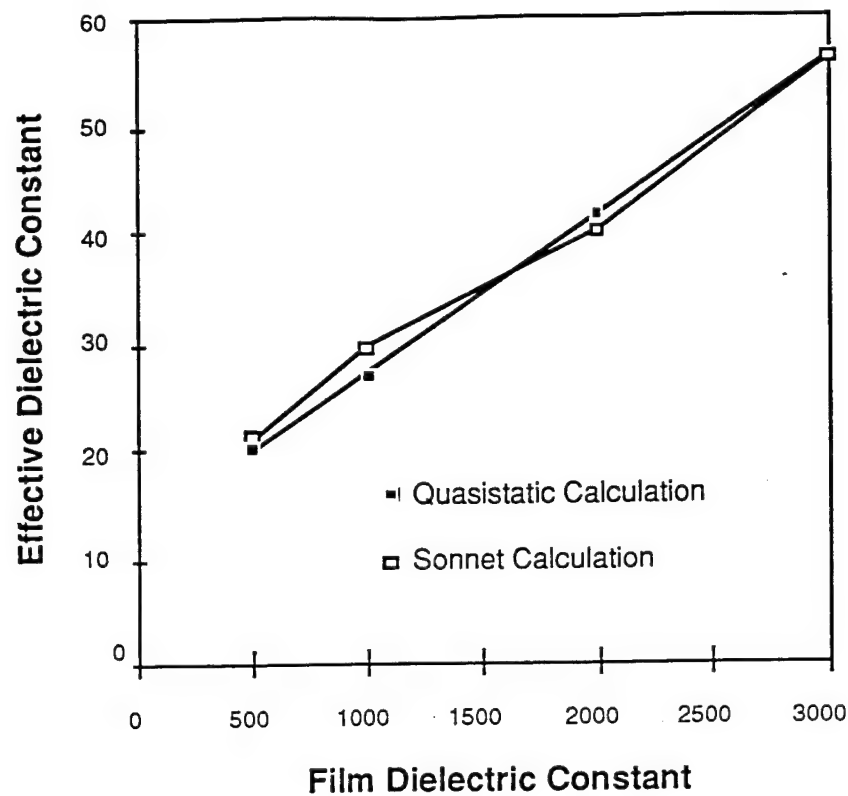


Figure 4.4-16. Comparison of SONNET and quasistatic models. Plot of effective dielectric constant ϵ' versus film dielectric constants that is independent of film loss tangents. The SONNET calculation (open squares) is at 20 GHz for $s=10\ \mu\text{m}$, $w=19\ \mu\text{m}$, and $t=0.3\ \mu\text{m}$.

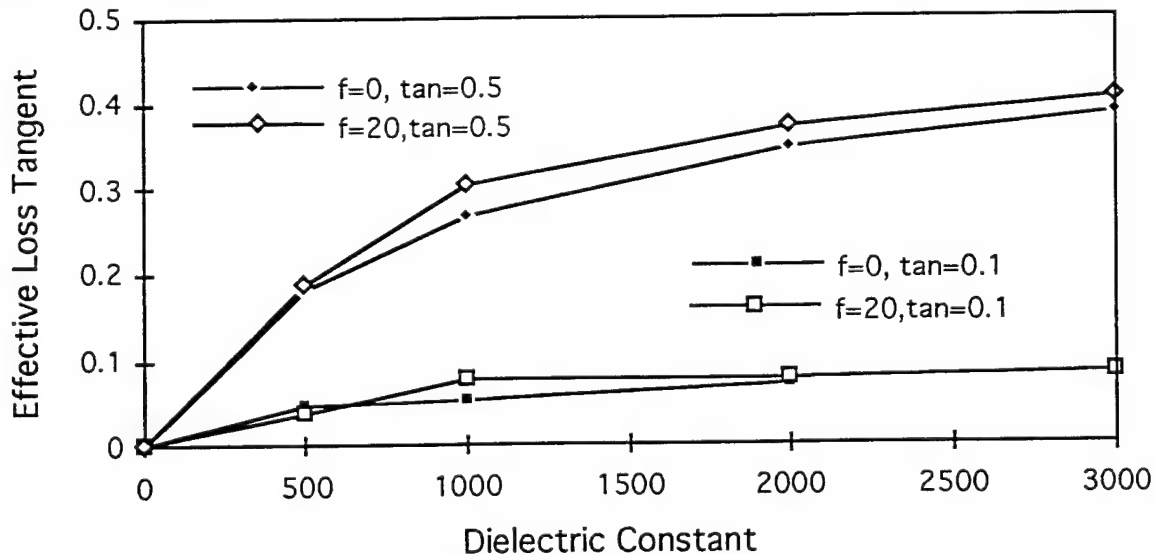


Figure 4.4-17. Comparison of SONNET and quasistatic models. Plot of effective loss tangent versus film dielectric constants for different film loss tangents calculated by a quasistatic model and by SONNET at 20 GHz for $s=10\ \mu\text{m}$, $w=19\ \mu\text{m}$, and $t=0.3\ \mu\text{m}$.

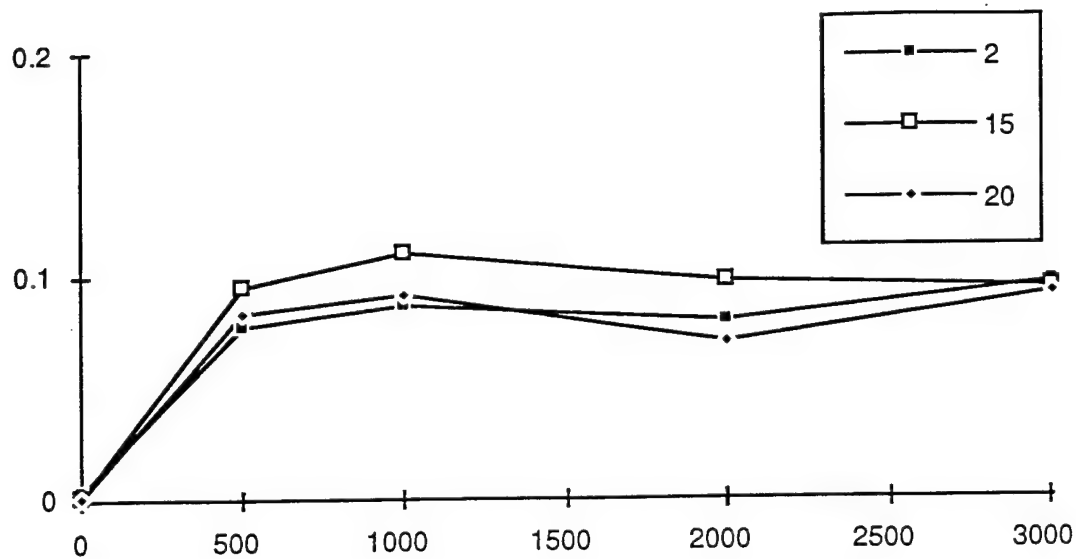


Figure 4.4-18. Frequency dependence of effective loss tangent dependence versus film dielectric constants for film loss tangent $\tan(\delta)=0.1$. Based on a SONNET calculation for $s=10\text{ }\mu\text{m}$, $w=19\text{ }\mu\text{m}$, and $t=2.0\text{ }\mu\text{m}$ at 2, 15 and 20 GHz.

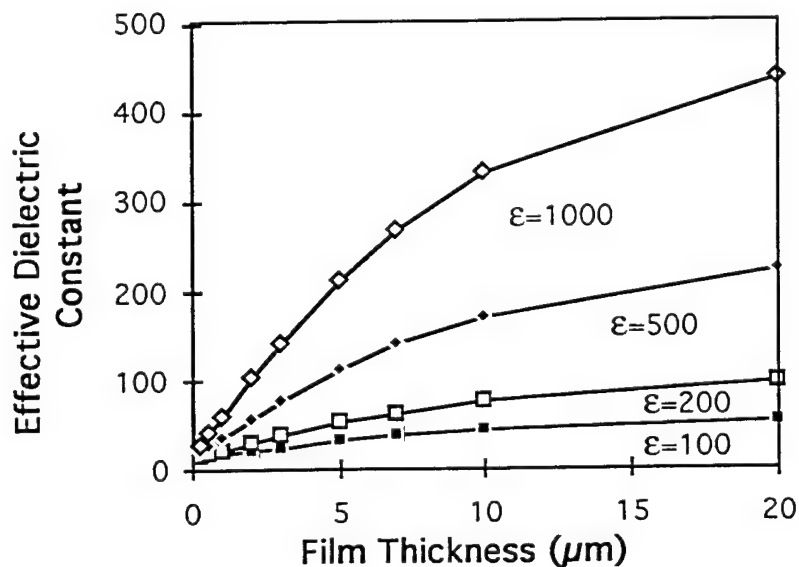


Figure 4.4-19. Plot of effective dielectric constant versus film thicknesses for different film dielectric constants. Based on a quasistatic calculation for $s=10\text{ }\mu\text{m}$ and $w=19\text{ }\mu\text{m}$.

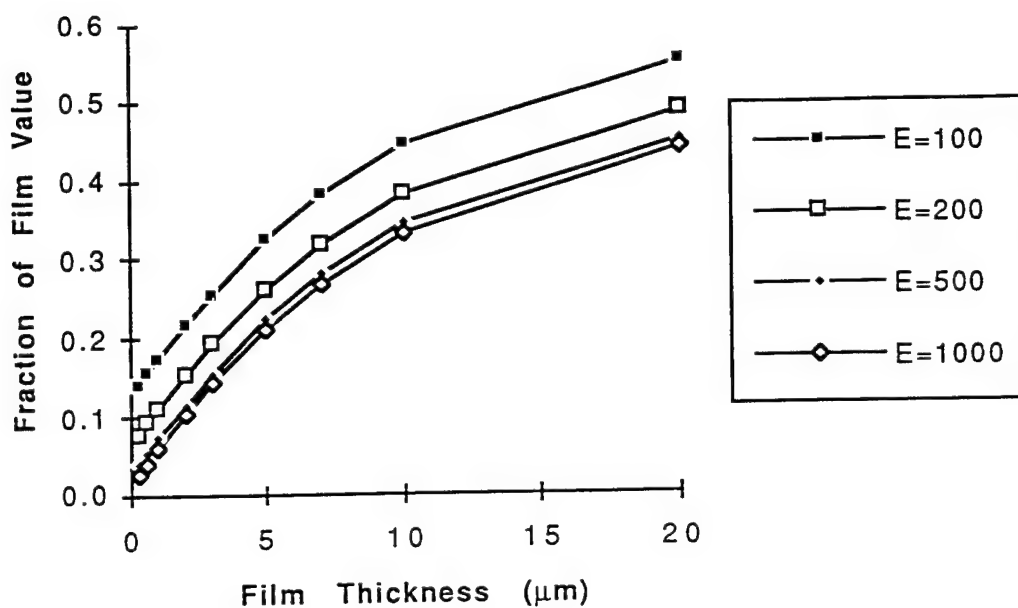


Figure 4.4-20 Plot of the ratio of the effective dielectric constant over the film dielectric constant versus film thicknesses for different film dielectric constants. Based on a quasistatic calculation for $s=10\text{ }\mu\text{m}$, and $w=19\text{ }\mu\text{m}$.

Circuit Design

This section describes the design and performance of a broadband coplanar waveguide (CPW) phase shifter combining the low loss of high temperature superconductors and the variable dielectric constant of ferroelectrics. Data on the measured phase shift will be presented, and a quasistatic filling factor model to calculate the impedance and effective dielectric constant will be presented.

The phase shifter consists of a coplanar waveguide transmission line. Figure 4.4-4 shows a cross section of the HTS/ferroelectric structure tested in for this paper. Pulsed laser deposition covers a LaAlO_3 substrate with a 0.3 nm thick YBCO film. After the HTS film is ion-milled, a laser ablation technique deposits the 0.3 nm thick ferroelectric film. Via windows are defined by removing part of the ferroelectric film, exposing the underlying HTS. Silver contact pads are deposited and patterned onto the exposed HTS providing an adequate microwave contact area.

There are a number of design considerations that need to be taken into account when developing an HTS/ferroelectric phase shifter. It is important to choose a transmission line topology that accentuates the best characteristics of the HTS and the ferroelectric materials. From a ferroelectric point of view, small gaps must be used to obtain a significant phase shift because: 1) the effective dielectric constant is larger for smaller gaps (the important parameter is the ratio of the film thickness to the gap width), 2) the ferroelectric dielectric constant depends on the electric field in the material (smaller gaps lead to larger electric fields for a given voltage). The smaller gap g and linewidth s confine a larger percentage of the energy in the ferroelectric film. A small gap leads to a trade-off: small gaps increase ohmic losses while they increase ferroelectric phase changes. Such a narrow gap topology would not be practical or feasible using conventional metals, since the ohmic losses in the conductors would be prohibitive. The use of HTS reduces ohmic losses compared to normal metals, and is a prime factor which enables the development of an HTS/ferroelectric phase shifter.

The required CPW linewidth is very small (less than 30 μm), so we designed a geometric taper to maintain 50 ohms while going from a large linewidth (suitable for microwave connector mounting) to the small linewidth needed for a phase shifter, shown in Figure 4.4-21. The linewidth and gap sizes were calculated from standard equations. It is interesting to note that the ratio of s/g is not constant along the taper.

At $s=10\text{ }\mu\text{m}$ the ratio is 0.526, while at $s=300\text{ }\mu\text{m}$ the ratio is 0.718. When the $508\text{ }\mu\text{m}$ LaAlO_3 substrate thickness (with a dielectric constant of 24.5) is comparable to the largest gap size, finite substrate thickness effects are observed in the change in the ratio.

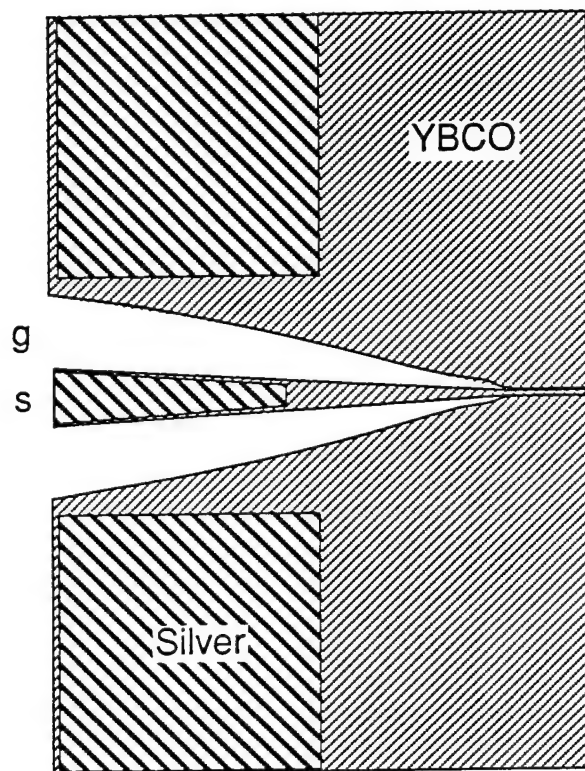


Figure 4.4-21. Top view of CPW HTS ferroelectric phase shifter. Without the dielectric, the CPW structure is a constant impedance transformer. The gap g and linewidth s are shown. Silver contacts are used to contact the YBCO.

Depositing a high dielectric constant film onto a coplanar waveguide structure changes the effective dielectric constant and impedance. It is important to note that the dielectric constant of the deposited ferroelectric film is greater than 100. The change in effective dielectric constant is negligible in regions with wide gaps; for small gaps, larger changes occur. To calculate the change in impedance and dielectric constant, the quasistatic calculation described in the previous section was employed, and the results were compared to simulations run on a commercial software program EM Sonnet. This quasistatic model provides a good basis for the design and analysis of the structures of interest. Figures 4.4-16 and 17 show a comparison of the two calculations. The close agreement of the two calculations shows that it is possible to use the quasistatic technique to predict the dielectric constant and impedances. This analysis has been used to determine the dielectric constant of a film on a CPW resonator.

The HTS/ferroelectric chip was mounted on a 3 mm thick teflon block, in a 6 mm wide channel. Conductive epoxy connects the transmission line and ground. Coax connections were made with K-connectors. We controlled the phase shifter with the external bias feature of the HP8720 network analyzer. Temperature was varied in an exchange gas system.

The insertion loss vs. temperature and frequency, Figure 4.4-22a, is less than 3 dB at 20 GHz. At higher temperatures, the larger insertion loss may be due to increases in the HTS film surface resistance, but it is more likely due to the ferroelectric losses. The ripple, shown in Figure 4.4-22a, is attributed to mismatch; a longer taper, or a design incorporating the effects of the dielectric film may reduce the ripple. No dc blocks are built into the design, future work should develop a broadband internal bias structure.

Power-dependent effects were not observed up to -10 dBm; higher powers need to be investigated to verify that the power handling of the phase shifter is limited by the superconducting film, as opposed to the ferroelectric film.

The change in phase shift and insertion loss at 10 V bias voltage and over the frequency band plotted in Figure 4.4-22b show that the effective dielectric constant changes uniformly up to 20 GHz. The roll-off frequency has not been determined, but for the 2-18 GHz band, SrTiO₃ will work very well. The insertion loss, shown in Figure 4.4-22a, changes by less than 1 dB. The change in insertion loss shows ripples that are attributed to impedance mismatch at the input and output.

Figure 4.4-23 shows a broad maximum around 60 K in the change in phase shift with applied voltage vs. temperature. These curves show the change in dielectric constant compared to the unbiased value as a function of temperature. The data may show a slight change in the maximum temperature with bias voltage. An important feature of the peak is that it is a broad maximum, meaning that temperature regulation is not too critical. The exact shape of these curves, and the peak temperature, changes with ferroelectric deposition parameters; more work must be performed to determine the reproducibility and sensitivity to deposition and processing conditions.

Figure 4.4-24 shows the phase relative to phase at zero bias voltage. As the voltage is increased, the phase shift changes in a parabolic fashion. At the highest voltage, there is some sign that the phase shift is approaching a maximum value. The phase

shift also depends on the previous state of the device. It has not been determined if this is due to hysteretic effects, or some other mechanism such as glass like behavior. This behavior persists above the peak in dielectric constant, in a region expected to be paraelectric.

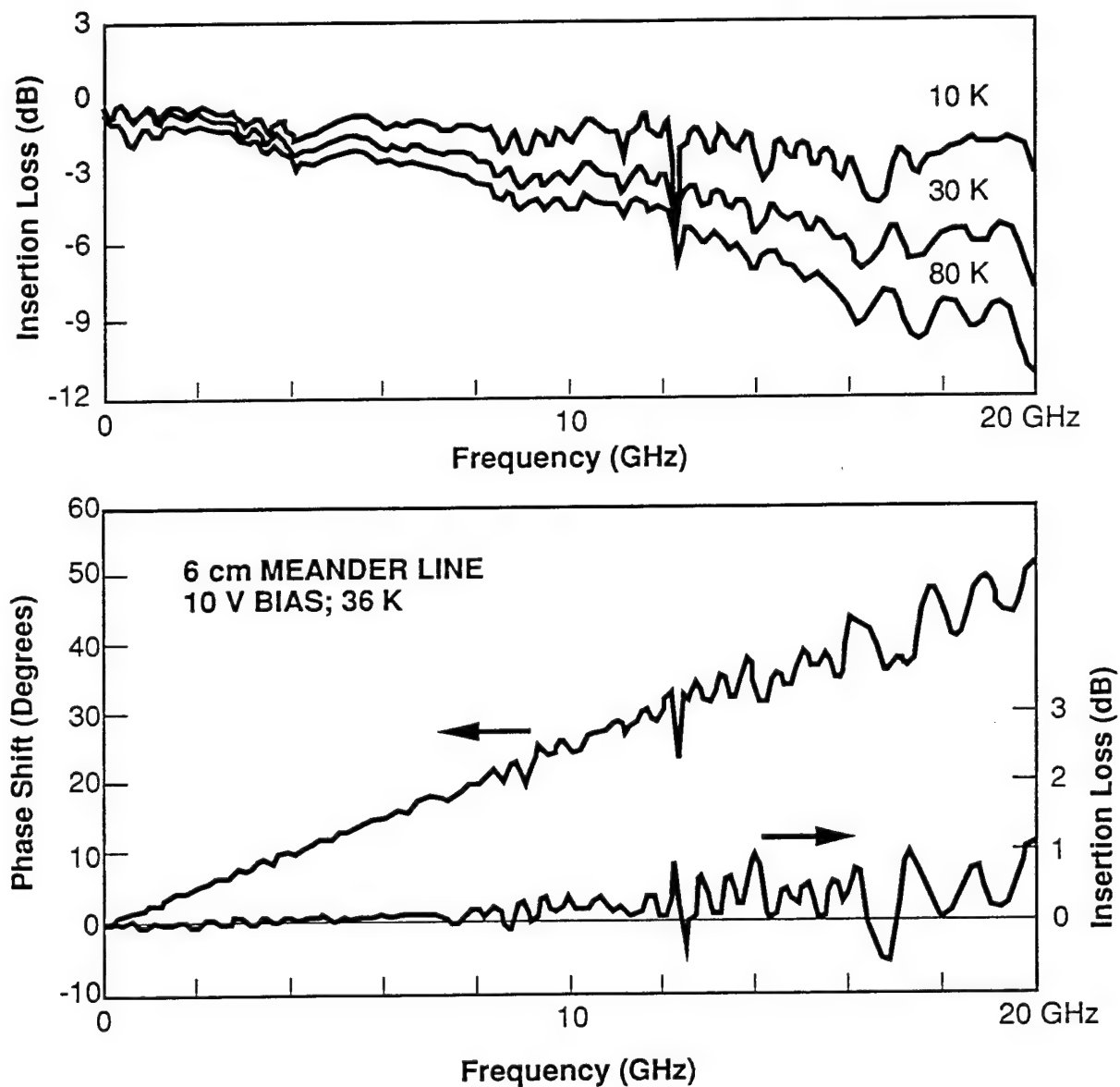


Figure 4.4-22. Performance over a broad band a) Insertion loss vs. frequency at three temperatures. The increase in insertion loss is probably due to damaged HTS. b) Change in insertion loss and phase vs. frequency at a bias of 10 V.

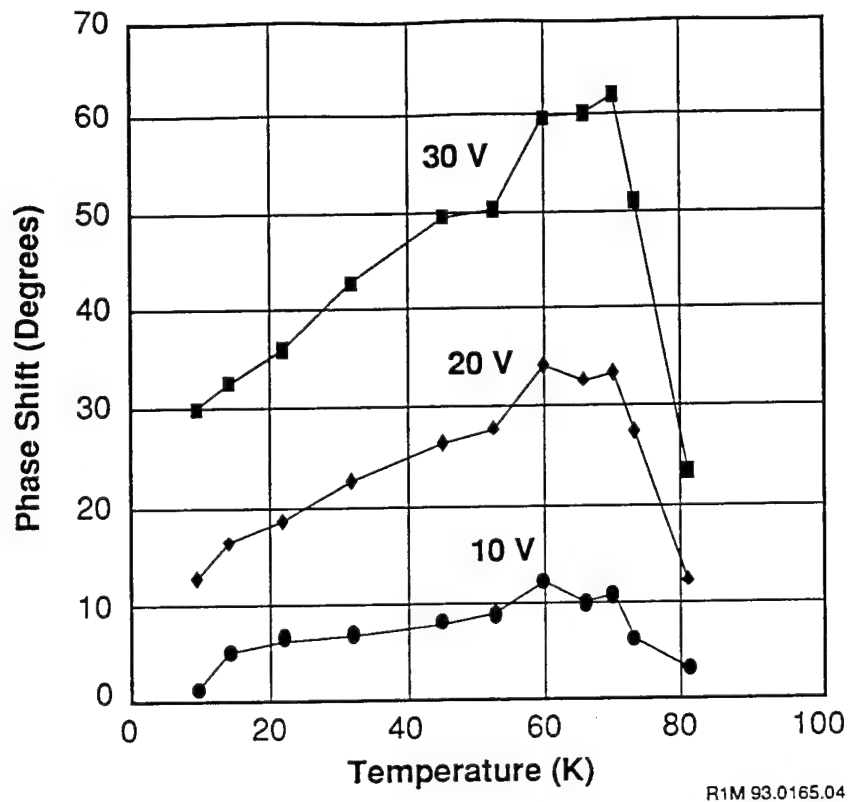


Figure 4.4-23. Phase shift vs. temperature for three different bias voltages.

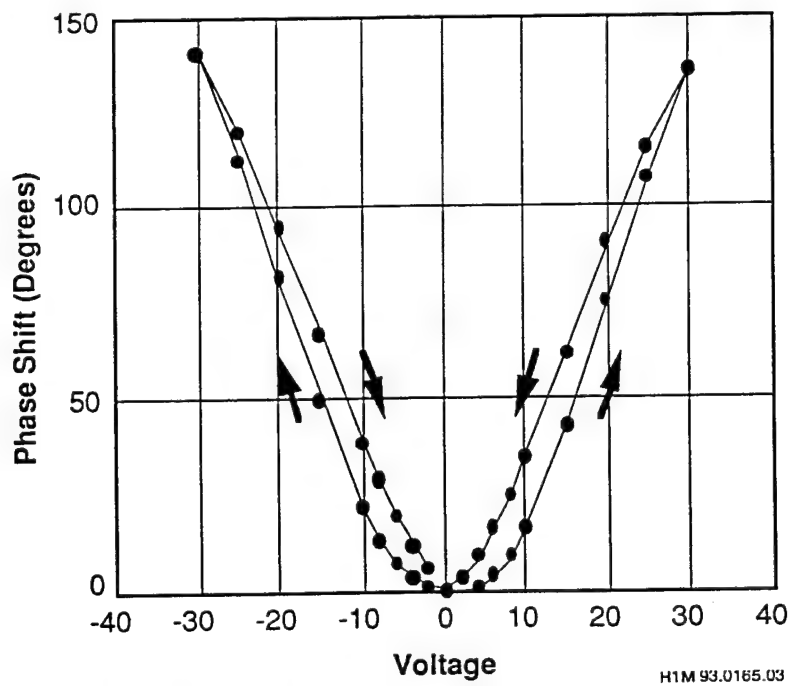


Figure 4.4-24. Phase shift vs. bias voltage at 20 K and 10 GHz.

Conclusion-Summary of Design Considerations

This section has described a broadband CPW phase shifter combining the low loss of high temperature superconductors and the variable dielectric constant of ferroelectrics is described. A phase shift of 80 degrees at 10 GHz with a 30 V bias has been demonstrated. A quasistatic filling factor model has been compared to more sophisticated techniques with excellent agreement. The phase shifter shows low insertion loss, and uniform time delay between 2 and 18 GHz.

The quasistatic model and the SONNET model give good agreement on the value of the effective dielectric constant (Fig. 4.4-16) and reasonable agreement for the effective loss tangent (Fig. 4.4-17). The effective dielectric constant is smaller for larger gaps, and the loss is smaller for larger gaps (based on filling factor calculations), thinner films, and lower loss films. Finally, as the thickness of the film increases, the effective dielectric constant increases, but the increase is less than linear for thicker films.

5. Cryocooler Subsystem Demonstration

This section describes the integration of a phase shifter (developed by this project) with a miniature flight qualified Stirling Cryocooler. The cryocooler will be described, and the beam steering demonstration will be discussed. The phase shifter design, fabrication, and test was described earlier. The demonstration of a HTS/ferroelectric phase shifter integrated with a cooler is one step toward the demonstration of a four-channel cooled phased array antenna. The cooled portion of such a system could be as compact as the system shown in Figure 5-1, a four channel phase shifter demonstration.

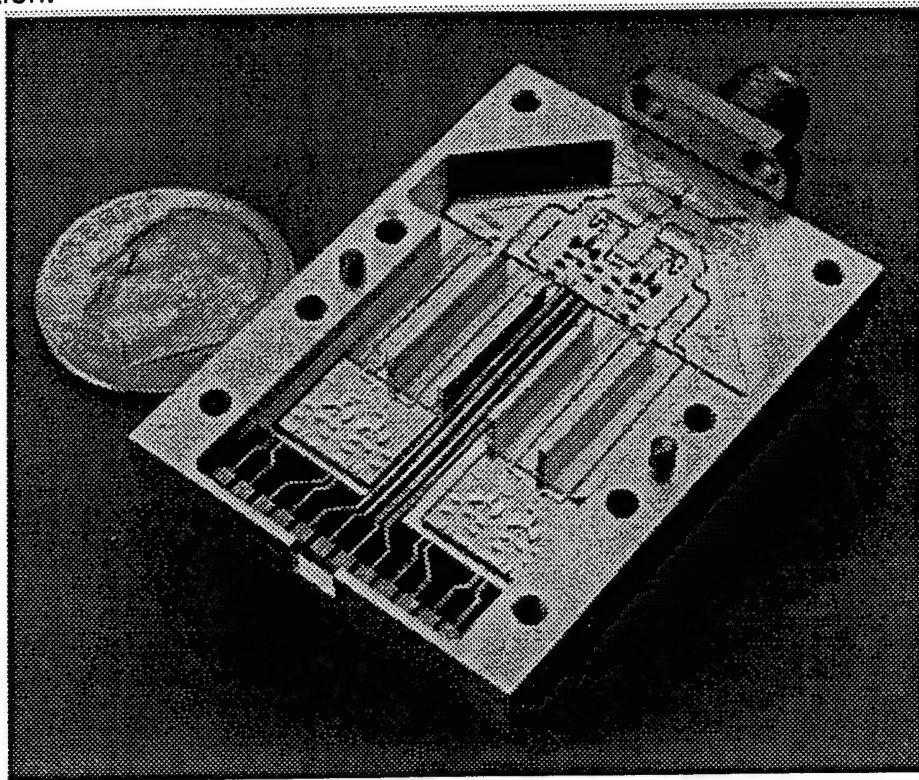


Figure 5-1 Compact four channel phase shifter test circuit which demonstrates illustrates that a four channel phased array can be very compact.

5.1 Cryocooler Operation

The TRW Stirling Cryocooler design used for this subsystem demonstration (Figure 5-2a) has been developed for space applications where compact size, low weight, low power consumption, high efficiency, and long life are important properties. A microwave circuit was mounted in the cryocooler, Figure 5-2b. The weight of the

cooler is 1.4 kg, the power is <12 Watts (to the mechanical cooler), and the mean time to failures is estimated to be 10 years with >95 % confidence. This design has been space qualified, and the thermal load depends on the operating temperature, as shown in Figure 5-3.

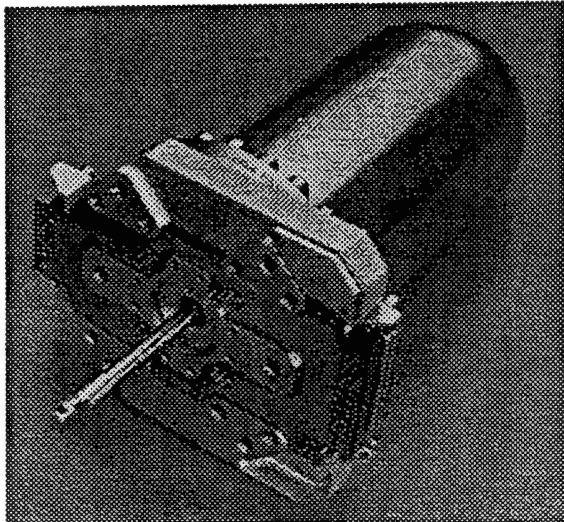


Figure 5-2a Miniature integrated Stirling cryocooler

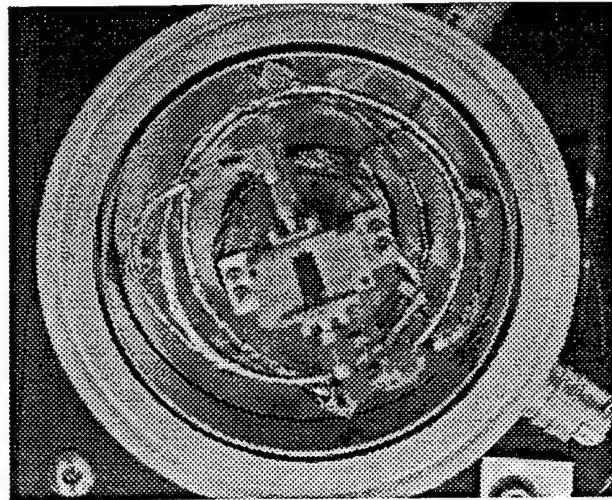


Figure 5-2b Phase shifter mounted to cryocooler in a compact vacuum chamber.

Figure 2b shows a microwave circuit mounted in a vacuum chamber that surrounds the cold tip of the cryocooler. Thin sheets of multilayer-insulation (MLI) surround the microwave circuit to reduce the radiative heat leak. Special thin wall stainless steel coax (3 mil thick, outer diameter 72 mils) with a stainless steel center conductor was used to get the microwave signal in and out of the chamber. The thermal properties of this coax are good, but the microwave insertion loss was not optimal. The insertion loss of a 33 cm length was 5 dB at 10 GHz; a 10 cm length would have 1.5 dB insertion loss. The thermal load of the coax is estimated to be about 6 mW per coax, for a total of 12 mW.

For applications with low insertion loss requirements, other coax cables are available. One option is a cable developed by Superconductor Technologies Incorporated with an insertion loss of .075 dB/cm and a thermal load of 0.069 W•cm. A 10 cm piece of cable has 0.75 dB insertion loss and a 6.9 mW thermal load.

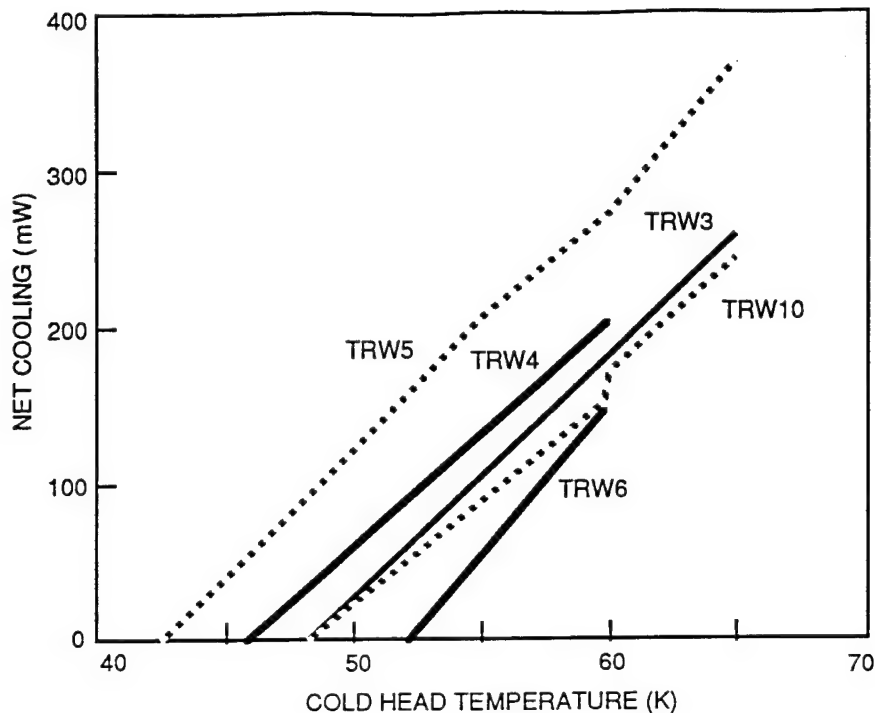


Figure 5-3 Load Line Data shows data on five coolers that have been assembled.

The cryocooler controller electronics changes the amplitude of the compressor piston motion to maintain constant temperature. Trip circuits prevent the cooler from experiencing any mechanical damage. The large thermal mass of the microwave circuit took about 10 hours to cool from room temperature down to 77 K, the operating temperature.

5.2 Beam Steering Demonstration

The integration of a microwave HTS circuit with a cryocooler is not a simple task. Hence, the purpose of this demonstration is to prove that it is possible to operate an HTS circuit with a cryocooler.

The block diagram of the demonstration is shown in Figure 5-4. A sketch is shown in Figure 5-5, and a photograph in Figure 5-6. The 10 GHz signal is split with a 3-dB power splitter. One channel goes to the cooled phase shifter, while the other goes to a variable attenuator to equalize the power sent to the two patch antennas.

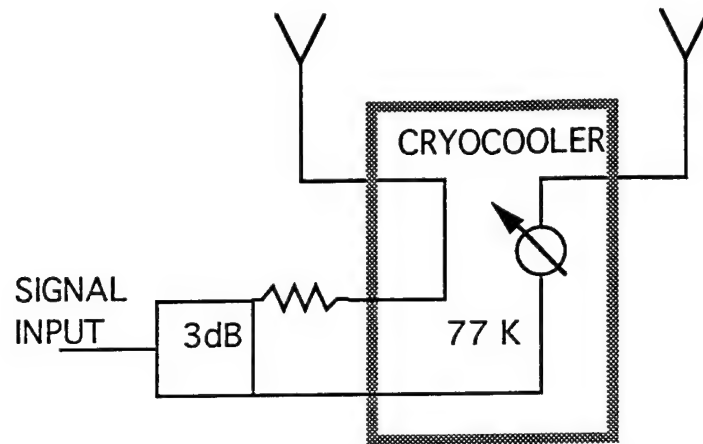


Figure 5-4. Block diagram of two -antenna beam steering demonstration.

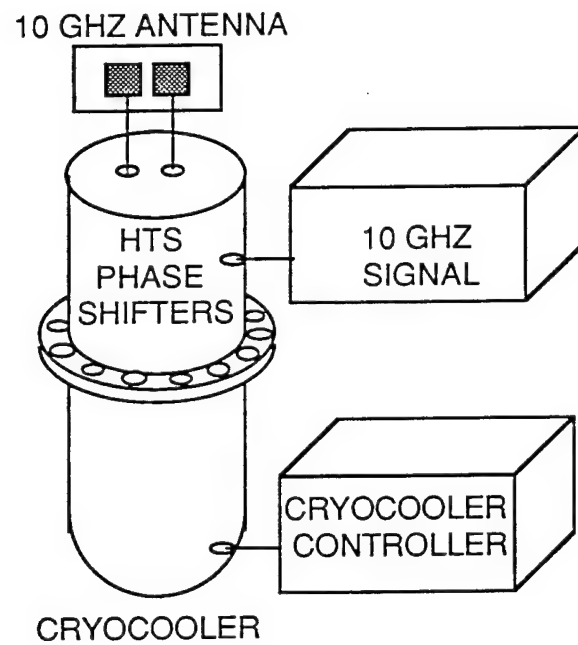


Figure 5-5. Schematic sketch of the two-antenna beam steering demonstration.

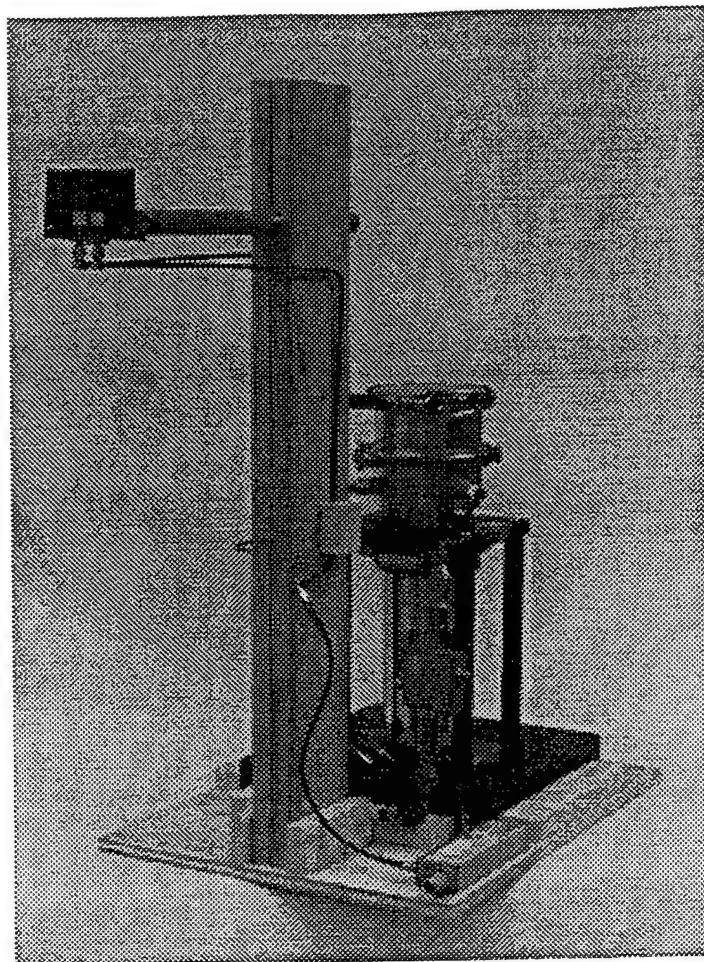


Figure 5-6. Photograph of the cryocooler and two patch antennas.

Patch antennas designed using standard equations, were fabricated and tested with performance close to the design parameters. The center frequency of the antenna was 10 GHz, and the bandwidth was about 500 MHz. The phase shifter developed by this program is very broadband, so the narrow bandwidth of the patch antennas limited the frequency range of operation.

The signal was detected by a network analyzer or a power meter. The 10 GHz signal power out of the network analyzer was 10 dBm. Either detector was fed by another patch antenna followed by an amplifier (with 27 dB gain) and a 200 MHz bandpass filter.

Two devices were measured. For one device, the phase shift as a function of applied voltage is shown in Figure 5-7. A linear response is obtained over most of the control

voltage range. Different devices have different responses. A plot of detected amplitude at different angles for two control voltages is shown in Figure 5-8. Figure 5-9 shows a plot of the antenna null position vs control voltage. A plot of the antenna amplitude vs control voltage is shown in Figures 5-10 and 11. Figure 5-12 shows the amplitude for a number of different control voltages.

Another device was measured, and data is plotted in Figures 5-13 through 15; Figure 5-13 the antenna amplitude at two control voltages; Figure 5-14 the antenna null position for different control voltages; Figures 5-15 and 16 the antenna amplitude at different angles

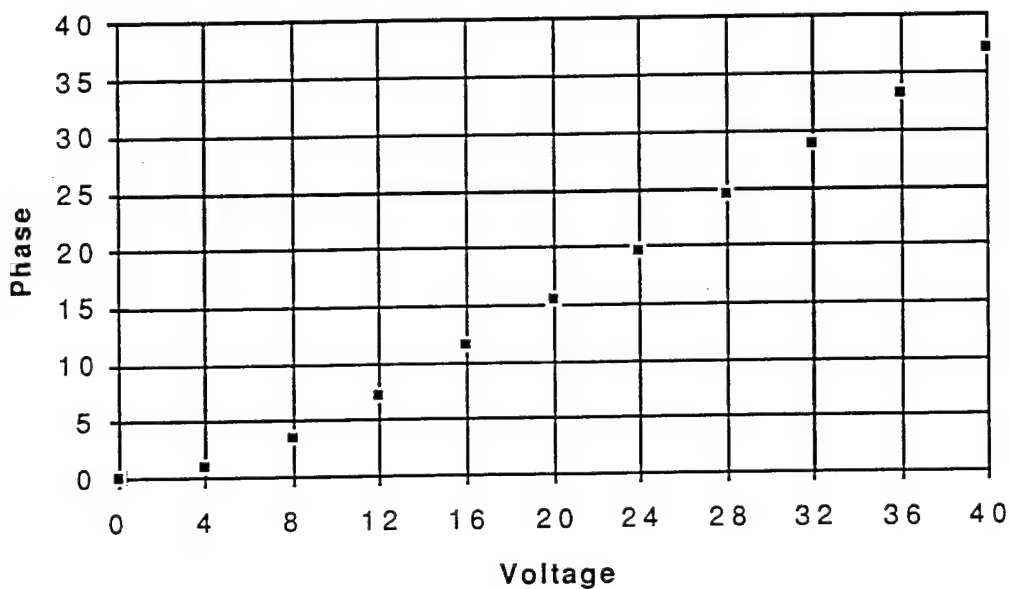


Figure 5-7. Phase vs. control voltage.

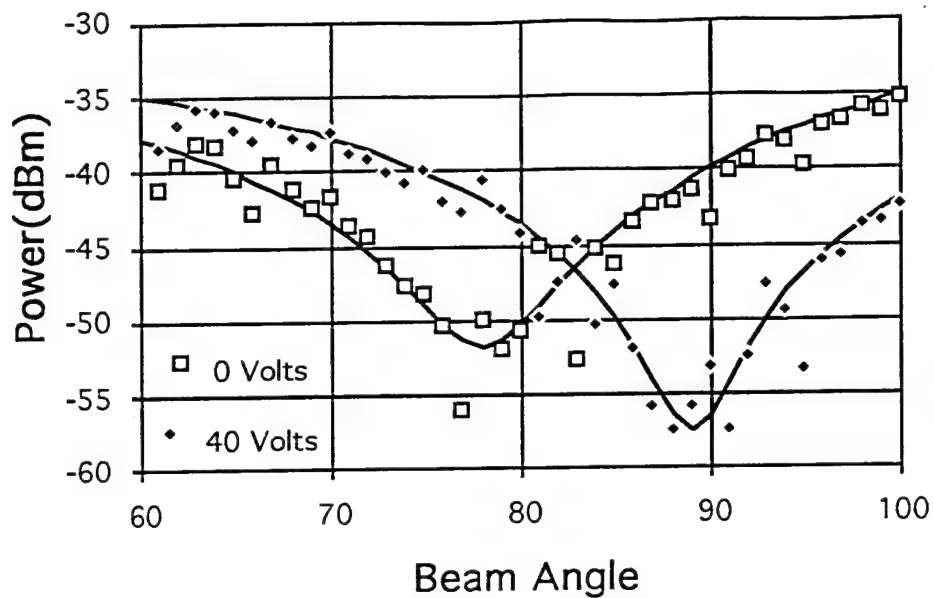


Figure 5-8. Amplitude vs. angle for two control voltages

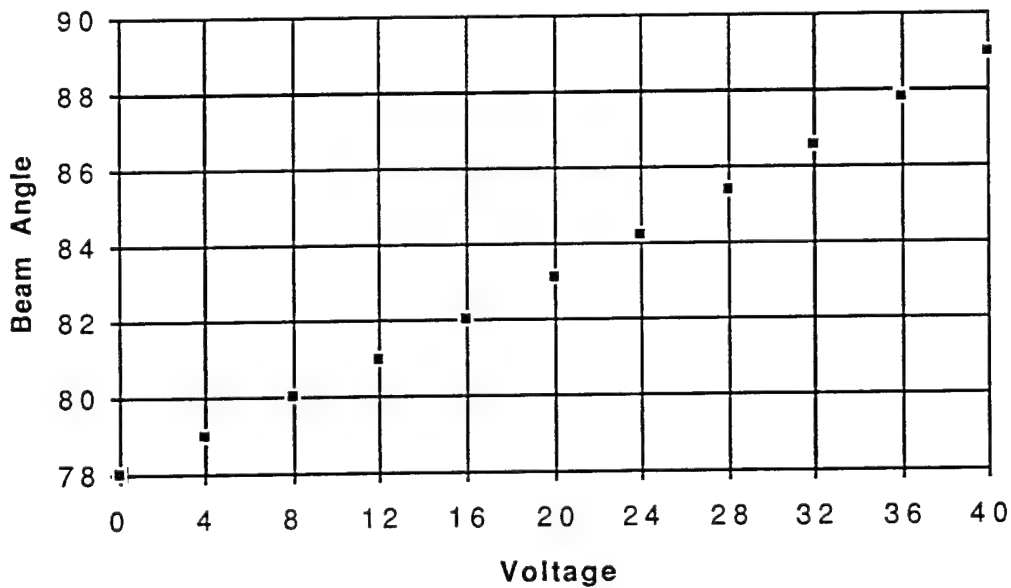


Figure 5-9. Antenna null position vs control voltage.

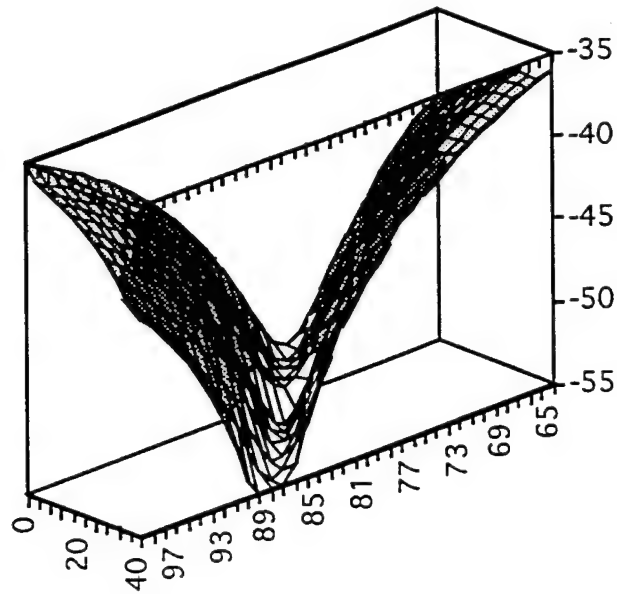


Figure 5-10. 3-D Plot of antenna amplitude vs. control voltage

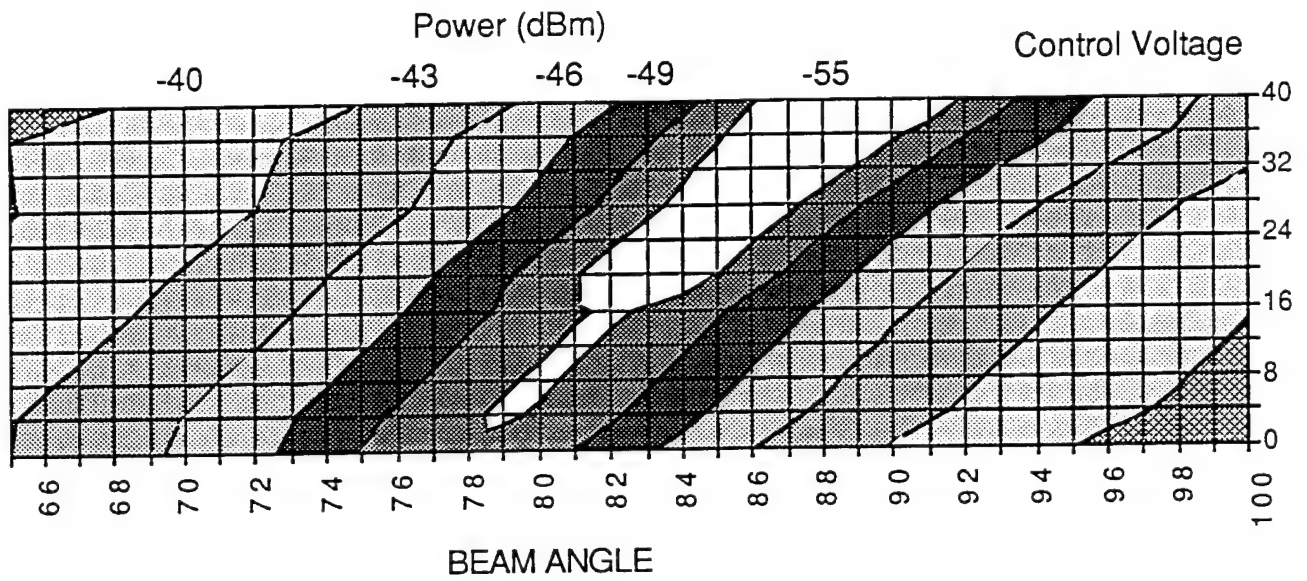


Figure 5-11. Topographic plot of antenna amplitude vs. control voltage. (same as Figure 5-10)

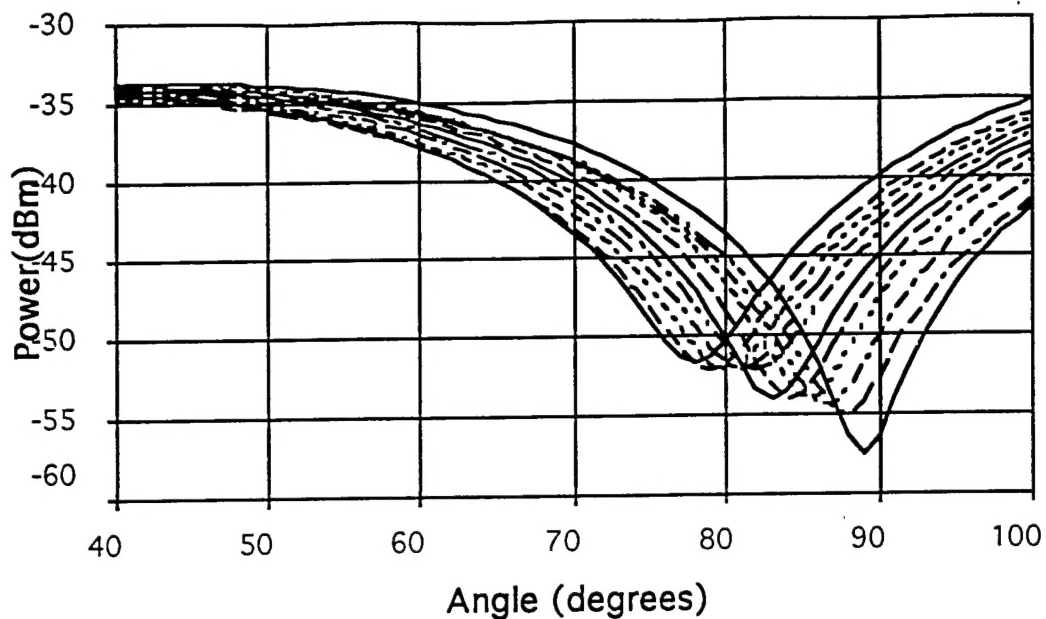


Figure 5-12. Fit to the antenna amplitude for various control voltages

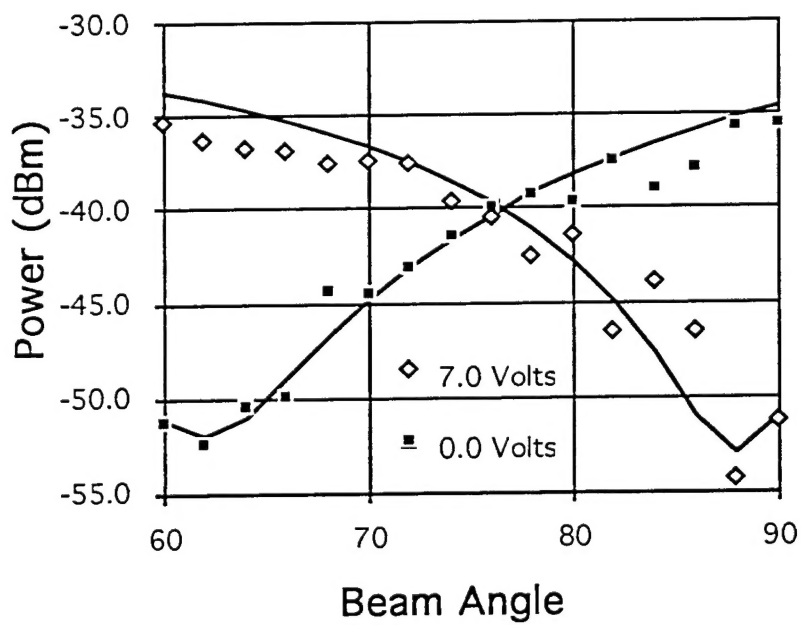


Figure 5-13. Amplitude vs. angle for two control voltages for another device.

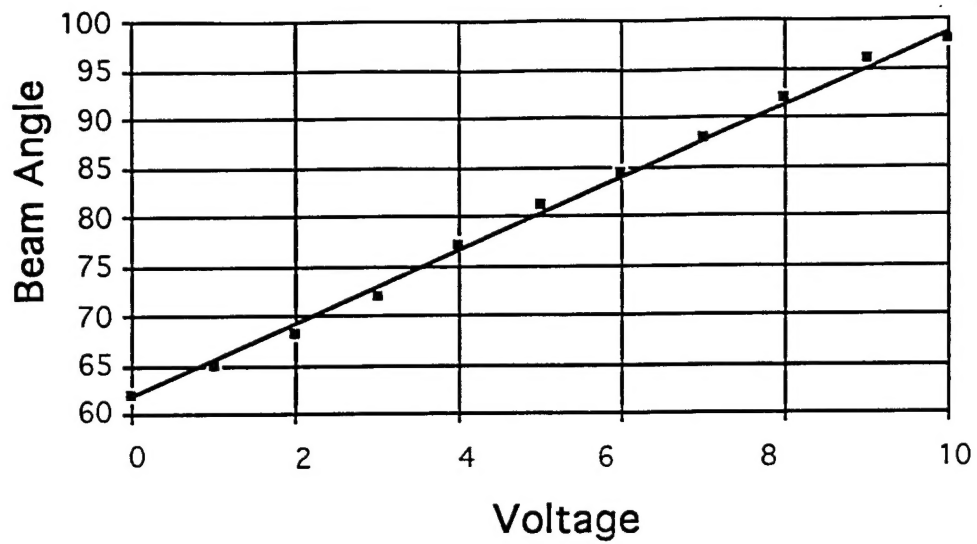


Figure 5-14. Antenna null position vs control voltage for another device.

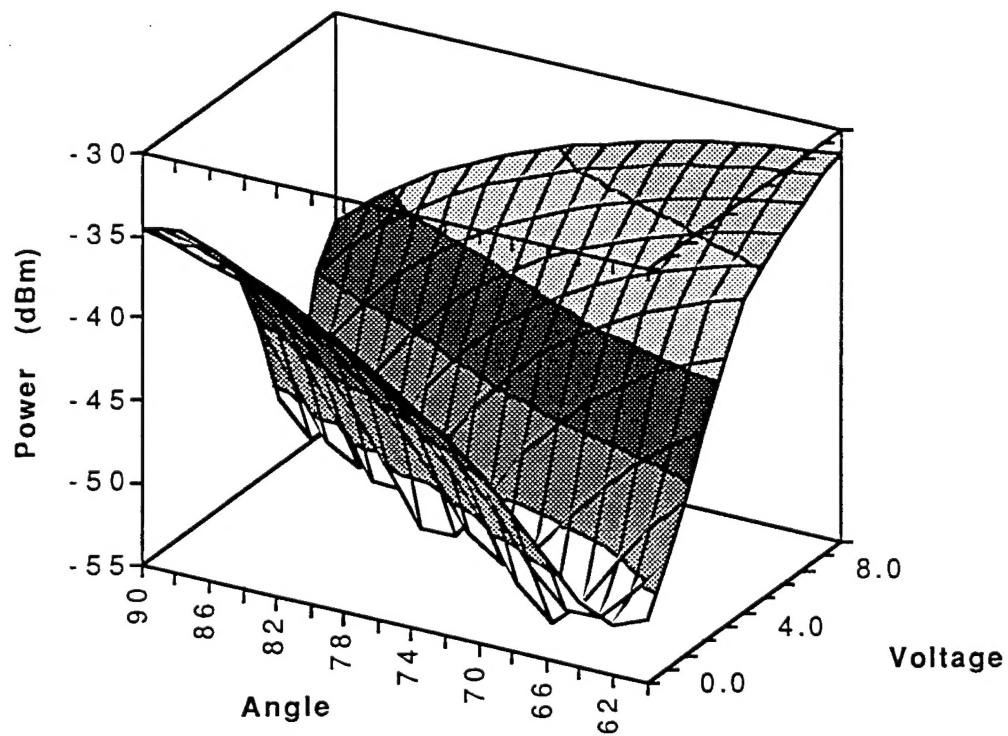


Figure 5-15. 3-D Plot of antenna amplitude vs. control voltage

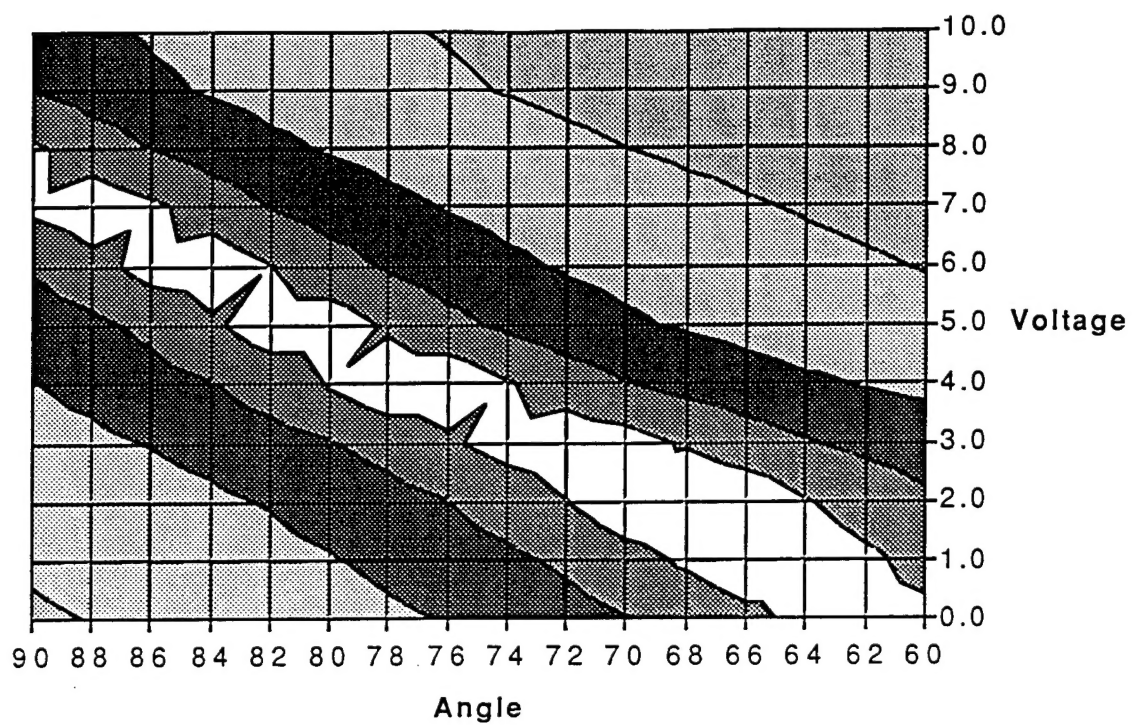


Figure 5-16. Topographic plot of antenna amplitude vs. control voltage for another device. (Same data as figure 5-15)

6 Further Developments

The design and test of the power combiner/splitter, the 90° Hybrid coupler, and the integrated monopulse network in a microstrip HTS format has demonstrated the improved performance possible with HTS circuits. The two antenna beam steering demonstrations of the HTS/Ferroelectric phase shifter has exhibited an ultra-wide bandwidth phase shifter. Better design tools are required to allow accurate microstrip circuit designs that use the LaAlO_3 substrate and YBCO HTS film as circuit components. These possible research areas have been identified.

- 1) Research directed at finding a suitable substrate with a lower dielectric constant.
- 2) Research directed at the development of new geometries using thin films (both epitaxial and spin-on) to enable new broad-band couplers.
- 3) Research directed at developing new models suitable for narrow gaps, high dielectric constants, and multilayer structures.
- 4) Research directed at demonstrating the HTS/Ferroelectric a 4 channel linear phased array.

It is recommended that the first four areas be pursued in the future. Once a microstrip HTS process is mature the goal of the development of a miniaturized HTS EW system suitable for aircraft and missiles will be achievable.